

## Probing progression of heating through the lower flare atmosphere via high-cadence IRIS spectroscopy

JURAJ LÖRINČÍK,<sup>1,2</sup> VANESSA POLITO,<sup>2,3</sup> GRAHAM S. KERR,<sup>4,5</sup> LAURA A. HAYES,<sup>6,7</sup> AND ALEXANDER J. B. RUSSELL<sup>8</sup>

<sup>1</sup>Bay Area Environmental Research Institute, NASA Research Park, Moffett Field, CA 94035, USA

<sup>2</sup>Lockheed Martin Solar & Astrophysics Laboratory, Org. A021S, Bldg. 203, 3251 Hanover St., Palo Alto, CA 94304, USA

<sup>3</sup>Department of Physics, Oregon State University, 301 Weniger Hall, Corvallis, OR 97331

<sup>4</sup>Department of Physics, Catholic University of America, 620 Michigan Avenue Northeast, Washington, DC 20064, USA

<sup>5</sup>NASA Goddard Space Flight Center, Heliophysics Science Division, Code 671, 8800 Greenbelt Road, Greenbelt, MD 20771, USA

<sup>6</sup>European Space Agency (ESA), European Space Research and Technology Centre (ESTEC), Keplerlaan 1, 2201 AZ Noordwijk, The Netherlands

<sup>7</sup>Astronomy & Astrophysics Section, School of Cosmic Physics, Dublin Institute for Advanced Studies, DIAS Dunsink Observatory, Dublin D15XR2R, Ireland

<sup>8</sup>School of Mathematics & Statistics, University of St Andrews, St Andrews, KY16 9SS, UK

### ABSTRACT

Recent high-cadence flare campaigns by the Interface Region Imaging Spectrograph (IRIS) have offered new opportunities to study rapid processes characteristic of flare energy release, transport, and deposition. Here, we examine high-cadence chromospheric and transition region spectra acquired by IRIS during a C-class flare from 2022 September 25. Within the flare ribbon, the intensities of the Si IV 1402.77 Å, C II 1334.53 Å and Mg II k 2796.35 Å lines peaked at different times, with the transition region Si IV typically peaking before the chromospheric Mg II line by 1 – 6 seconds. To understand the nature of these delays, we probed a grid of radiative hydrodynamic flare simulations heated by electron beams, thermal conduction-only, or Alfvén waves. Electron beam parameters were constrained by hard X-ray observations from the Gamma-ray Burst Monitor (GBM) onboard the *Fermi* spacecraft. Reproducing lightcurves where Si IV peaks precede those in Mg II proved to be a challenge, as only a subset of *Fermi*/GBM-constrained electron beam models were consistent with the observations. Lightcurves with relative timings consistent with the observations were found in simulations heated by either high-flux electron beams or by Alfvén waves, while the thermal conduction heating does not replicate the observed delays. Our analysis shows how delays between chromospheric and transition region emission pose tight constraints on flare models and properties of energy transport, highlighting the importance of obtaining very high-cadence datasets with IRIS and other observatories.

### 1. INTRODUCTION

Solar flares are characterized by a sudden increase of radiation across all wavelengths, from radio waves to gamma rays. The increase of radiation is a by-product of the release of energy stored in the magnetic field within the solar atmosphere, facilitated by magnetic reconnection. In the standard flare scenario (Carmichael 1964; Sturrock 1966; Hirayama 1974; Kopp & Pneuman 1976) and its extensions, energy released in the corona manifests in bulk flows, particle acceleration (e.g. Brown 1971; Lin & Hudson 1976; Holman et al. 2011), *in-situ* heating (e.g. Ricchiazzi & Canfield 1983; Czaykowska et al. 2001; Longcope 2014), and excitation of magnetohydrodynamic (MHD) waves (e.g. Emslie & Sturrock 1982; Fletcher & Hudson 2008; Russell & Fletcher 2013; Reep & Russell 2016; Kerr et al. 2016).

The time scales at which the lower solar atmosphere responds to the energy transfer processes vary depending on the mechanism. Early flare observations demonstrated correlations between hard X-ray (HXR) and microwave radio emission generated by accelerated non-thermal electrons and the H $\alpha$  line emission probed by various ground-based observatories (see e.g. Křivský 1963; Švestka 1970; Kane 1974; Lin & Hudson 1976; Zirin 1978, and references therein), suggesting that the accelerated electrons deposit their energy in the chromosphere. The chromosphere responds rapidly to electron bombardment, with more recent ground-based H $\alpha$  line observations acquired at time resolution of the order of seconds or less (e.g. Trottet et al. 2000; Radziszewski et al. 2007, 2011), revealing very short (down to < 3 s) time lags relative to HXR lightcurve maxima. Observations from the Solar

Maximum Mission showed that HXR signals also coincide in time with emission formed in the overlying transition region (e.g. Cheng et al. 1981; Poland et al. 1982; Tandberg-Hanssen et al. 1983). Unlike the ground-based  $H\alpha$  observations, the ultraviolet (UV) emission of ions forming therein (such as Si IV, C IV, O IV, O V) was initially observed at low spatial resolution, limiting the identification of emission sources. Valuable insights (see e.g. the review Fletcher et al. 2011, and references therein) into the spatial and temporal coherence between the lower-atmospheric emission and HXR sources were brought by the Transition Region and Coronal Explorer (TRACE; Handy et al. 1999). This imaging telescope provided excellent  $1''$  spatial resolution and cadence as high as 2 s. However, this cadence was only available with a single passband at a time, with no multi-temperature coverage (e.g. Hudson et al. 2006; Fletcher 2009; Liu et al. 2013).

Longer time lags of the order of 10 s, observed between  $H\alpha$  and HXR lightcurve maxima, were attributed to heating via thermal conduction following *in-situ* coronal energy release (e.g. Trotter et al. 2000; Radziszewski et al. 2007, 2011). Relatively-slower chromospheric response to this heating mechanism is given by the propagation of conduction fronts along reconnected field lines at ion sound speeds of a few  $100 - 1000 \text{ km s}^{-1}$ . Hereafter we refer to this scenario as ‘thermal conduction’ driven flares; thermal conduction of course plays a role in all flares, but here we refer to this as the dominant means by which energy is transported from the corona to the lower atmosphere. Another proposed energy transport mechanism that operates relatively slower compared to non-thermal particles are downward propagating Alfvén waves generated from the reconnection site. Alfvén waves travel from the corona at  $c_A = 10^3 - 10^4 \text{ km s}^{-1}$ , reaching the chromosphere within a few seconds of their generation (assuming this occurs at the apex of loops). Most of the Poynting flux dissipates through the transition region and chromosphere, but the location of the deposition depends on wave parameters and the ionization fraction (Haerendel 2009; Reep & Russell 2016; Reep et al. 2018). The Alfvén wave heating can effectively drive chromospheric emission (Kerr et al. 2016; Reep et al. 2018), however these models still require observational validation.

Building upon the extensive literature on the atmospheric response to flare energy deposition, relative timings of intensity enhancements of lines formed at different atmospheric depths can in principle trace the progression of heating throughout the solar atmosphere. Spectroscopic observations from the Coronal Diagnostic Spectrometer (CDS; Harrison et al. 1995) identified time lags at scales of minutes between emission formed at flare  $\approx 8 \text{ MK}$  and lower ( $0.01 - 0.1 \text{ MK}$ ) temperatures, enabling the differentiation between energy transport mechanisms (e.g. Brosius & Phillips 2004; Brosius & Holman 2010, 2012). However, a detailed diagnostics of heating propagation focused on the lower atmosphere, where the bulk of the flare radiative response originates at rapid timescales of seconds, remains largely unexplored. This is due to the lack of simultaneous observations of the chromosphere and transition region at very high, ideally sub-second, cadence and with sufficient spatial resolution.

Since 2013, unprecedented simultaneous observations of the chromosphere and transition region have been made possible by the Interface Region Imaging Spectrograph (IRIS; De Pontieu et al. 2014). By observing spectral lines formed at different heights in the lower atmosphere, IRIS provides invaluable flare diagnostics (see e.g. the review De Pontieu et al. 2021, and references therein). For instance, the transition region Si IV  $1402.77 \text{ \AA}$  and the chromospheric Mg II k ( $2796.35 \text{ \AA}$ ) and Mg II h ( $2803.52 \text{ \AA}$ ) lines are among the most commonly studied spectra formed in flaring conditions, often in tandem with HXR or microwave radio signatures of energetic electrons (e.g. Liu et al. 2015; Li et al. 2015; Warren et al. 2016; Brosius & Inglis 2018; Polito et al. 2023b). The newly-developed IRIS flare observing programs with cadence below 1 s, are particularly well-suited to study the rapid response of the chromosphere and transition region to flare energy deposition. These invaluable datasets have already been utilized in detailed studies of chromospheric condensation (Lörinčík et al. 2022; Wang et al. 2023). High-cadence IRIS observations of a C4-class flare from 2022 September 25 recently provided key evidence of slip-running reconnection manifested in super-Alfvénic apparent motions of flare ribbon kernels with velocities reaching thousands  $\text{km s}^{-1}$  (Lörinčík et al. 2025). Some of the kernels were also captured by the IRIS slit, providing spectral observations of different lines well suited to study the response of the chromosphere and the transition region to energy deposition simultaneously at very high cadence.

In recent years, IRIS observations are often used alongside flare simulations modeled with radiative hydrodynamic loop numerical models such as RADYN, HYDRAD, or FLARIX (see e.g. recent reviews by Kerr 2022, 2023). To model flare emission in such codes, energy can be injected in several ways: thermalization of non-thermal electron beams (e.g. Allred et al. 2005, 2015; Polito et al. 2023a), thermal conduction-only from flare heating of the corona (e.g. Testa et al. 2014; Polito et al. 2018), or an approximated form of dissipation of Alfvén waves (e.g. Kerr et al. 2016). Where and how fast the energy is deposited, the subsequent plasma response, and the resulting emission depends on the heating parameters and the initial physical conditions of the atmosphere. When modeled as a power-law energy distribution, the electron beam parameters include the power carried by non-thermal electrons,  $P_{NTE}$ , the electron spectral index,  $\delta$ , that describes its slope, and the minimum energy of the distribution, the low-energy cutoff  $E_c$ . For example, Allred et al. (2005) showed that in the atmosphere heated by strong non-thermal flux ( $F = 10^{11} \text{ erg cm}^{-2} \text{ s}^{-1}$ ), both chromospheric and transition region line intensities increase rapidly after the heating onset. Ca II k intensities however peak only after the chromospheric condensation fronts reach the lower chromosphere. Testa et al. (2014)

noted on differences between the response of the transition region and chromosphere to electron beam parameters. Among other, they found that Mg II intensities have much weaker dependency on small changes of  $E_c$  than those of the Si IV line. The nanoflare model investigation of [Polito et al. \(2018\)](#) showed that electrons can penetrate deeper into the atmosphere if loops have lower initial densities, thus driving a stronger plasma response to the heating in chromospheric and transition region lines, compared to that observed in denser loops for the same amount of energy released. Lastly, in addition to the parameters discussed above, the penetration depth of non-thermal electron beams can depend on  $\delta$ . [Allred et al. \(2015\)](#) nicely illustrate this in their analysis of the stratification of heating rates in different solar/stellar atmospheres. Overall, the more power is carried by higher energy electrons, the more deeply a particle beam penetrates.

In this study, we revisit the observations of the 2022 September 25 flare to study, for the first time, the stratified response of the lower atmosphere to flare heating on short timescales. We found intriguing delays between Mg II line intensity peaks relative to the Si IV and C II emission observed in a flare ribbon. Physical mechanisms causing these delays are investigated using a grid of RADYN simulations heated by different energy transfer mechanisms. The manuscript is structured as follows. Section 2 introduces datasets analyzed in Sections 3 and 4. Section 5 details the investigation of RADYN models and their comparison to the observations. The results of our analysis are discussed in Section 6 and summarized in Section 7.

## 2. DATA

### 2.1. Spectroscopic and imaging observations

In this study we analyze spectroscopic observations of a C4-class flare observed by IRIS on 2022 September 25. IRIS provides high-resolution spectroscopy in two far-ultraviolet (FUV, 1331.6 Å – 1358.4 Å and 1380.6 Å – 1406.8 Å) and one near-ultraviolet (NUV, 2782.6 Å – 2833.9 Å) bands. These bands contain a multitude of lines formed across a wide range of temperatures of  $\log(T \text{ [K]}) = 3.7 - 7$ , with spectral resolutions of 0.026 Å and 0.053 Å and spatial resolutions of  $\approx 0.33'' - 0.4''$ , in the FUV and NUV channels, respectively. The Slit-Jaw Imager (SJI) of IRIS provides context imaging observations with a field of view (FOV) of up to  $175'' \times 175''$ . The event under study was observed in a high-cadence flare observing program in the sit-and-stare mode with the temporal resolution of  $\approx 0.92$  s for spectra and  $\approx 1.8$  s for the SJI observations. Onboard spatial and spectral binning of 2 was used. The spectral observations were carried-out with exposure times of 0.3 s (FUV band) and 0.19 s (NUV band) in four spectral windows centered on the C II 1335 & 1336 Å lines, Si IV 1403 Å line, Mg II k 2796 Å line, and NUV continuum at 2814 Å. In addition to the spectral observations, the dataset contains SJI 2796 Å and 1330 Å imagery of the chromospheric and transition region emission, respectively. The IRIS observations were processed using packages available within the SolarSoft and `irispy_lmsal` software libraries. The level-2 science-ready IRIS observations were despiked and subsequently smoothed using a sliding boxcar to reduce the noise while preserving the overall trends (Section 4.1). The boxcar size was two pixels in the time dimension and 4 and 2 wavelength pixels in the FUV and NUV channels, respectively, as to account for the difference in the wavelength resolution between these channels. The spectra were finally normalized by exposure times. Using the `iris_orbitvar_corr_l2` routine we verified that no further wavelength correction due to IRIS orbital variations was needed.

We further investigated imaging observations of the event performed by the Atmospheric Imaging Assembly (AIA; [Lemen et al. 2012](#)) onboard the Solar Dynamics Observatory (SDO; [Pesnell et al. 2012](#)). AIA captures full-disk images of the Sun at a spatial resolution of  $\sim 1''.5$  at a cadence of 12 s and 24 s, depending on the filter channel. Snapshots from the AIA 131 Å channel, in flaring conditions dominated by the Fe XXI line emission ( $\log(T \text{ [K]}) = 7.05$ ) (e.g. [O'Dwyer et al. 2010](#)), were used to inspect flare loops forming during the event. Flare ribbons were studied in AIA 1600 Å observations ( $\log(T \text{ [K]}) = 5.0$ ) with a major contribution from the transition region C IV lines, Si I continua, as well as numerous chromospheric lines ([Simões et al. 2019](#)). The AIA observations were handled and visualized in the SunPy environment ([SunPy Community et al. 2020](#)). The full-disk AIA observations and SJI dataset were slightly misaligned. In order to co-align the two instruments, we determined the shift between the instrument coordinate systems based on comparing locations of bright ribbon emission observed in the SJI 1330 Å and AIA 304 Å as well as 1600 Å snapshots, while taking the AIA observations for reference. The shift between the instruments determined via this method was  $X = -2''.2$ ,  $Y = -2''.4$ .

### 2.2. SXR observations and Fermi/GBM spectroscopy

The soft X-ray (SXR) flux of the Sun was studied using data from the X-ray Sensor (XRS) onboard the GOES satellite. HXR observations from the Gamma-ray Burst Monitor (GBM; [Meegan et al. 2009](#)) onboard the *Fermi*/GBM space telescope were used to analyze the non-thermal electron sources during the flare. *Fermi*/GBM detects gamma rays and X-rays in the energy range between 8 keV and 40 MeV at the time resolution of 1 s. While both GOES and *Fermi*/GBM observe the Sun-as-a-star emission, no other flare above A class occurred in the time period under consideration. The GBM spectra were analyzed via

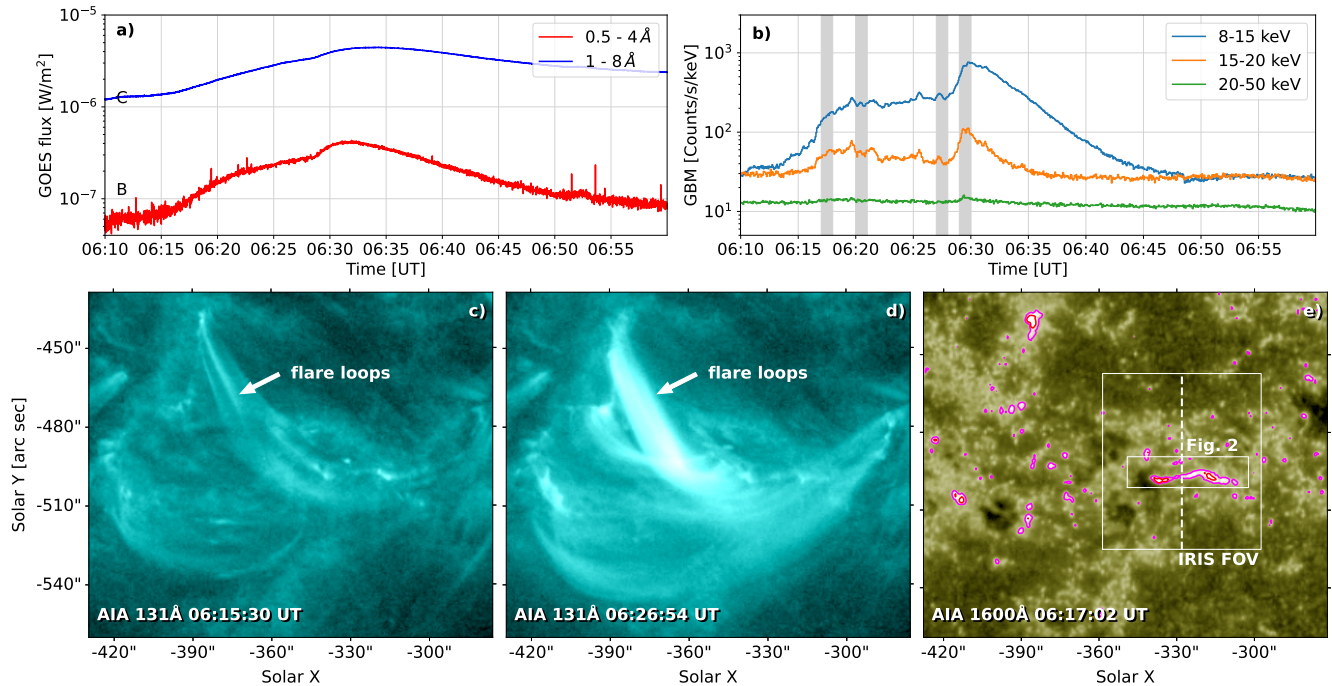


**Figure 1.** Context observations of the event. Panels a and b present flare SXR and HXR lightcurves measured in different wavelength and energy bands by GOES and *Fermi*/GBM, respectively. The grey stripes in panel b delineate time intervals of successful fits to the GBM spectra. Panels c – d present AIA 131 Å observations of flare loops developing during the flare. Observations of the flaring region in the 1600 Å channel of AIA with the IRIS FOV and the FOV of Figure 2 are shown in panel e. The magenta and red contours correspond to 30 and 50% of the maximal intensity.

the OSPEX software. We employed the `v_th` and `thick2` routines to fit spectra with thermal and thick-target bremsstrahlung models, respectively. The `thick2` model represents thick-target bremsstrahlung emission from a population of non-thermal electrons following a single power-law energy distribution. Background emission was subtracted from the spectra first. This was determined by fitting by a polynomial to pre- and post-flare time intervals where no flare emission was observed. Spectra were integrated over 1-minute long periods centered at 06:17:30, 06:20:30, 06:27:30, and 06:29:30 UT (grey stripes in Figure 1b). No traces of non-thermal emission were found before  $\approx 06:16$  UT, even using longer integration times. From this fitting we obtained  $\delta$ ,  $E_c$ , and the power carried by non-thermal electrons,  $P_{NTE}$ . Since *Fermi* does not image the X-ray sources, and therefore constrain the flare area  $A$ , which itself is necessary to obtain the non-thermal energy flux densities  $F = P_{NTE}/A$ , we opted to constrain the footpoint area via UV ribbon imagery (e.g. Rubio da Costa et al. 2015, 2016; Graham et al. 2020; Polito et al. 2023b). We first assumed that the energy released during the event was distributed to both ribbons defined by the 50% intensity contours in the AIA 1600 Å observations (red contours in Figure 1e), providing the upper area limit  $A_{\max}$  and thus the lower limit on  $F$ . The higher limit on  $F$  was determined from the area  $A_{\min}$  within bright kernels composing the southern ribbon observed in the 1330 Å channel of SJI. The 50% intensity level, designated by the red contours in Figure 2, was again used to delineate the pixels whose area was summed. The lower limit on  $A_{\min}$  was found to be  $< 10^{16}$  cm<sup>2</sup>, roughly equivalent to 17 IRIS pixels. The broad range of  $A$  listed in Table 1 thus accounts for the possibility of non-thermal energy distributed to both small-scale IRIS kernels as well as extended ribbon structures.

### 3. OVERVIEW OF THE EVENT

The C4-class flare under study occurred in the NOAA active region 13107 on 2022 September 25 and its context observations are presented in Figure 1. The time evolution of the SXR flux detected in the 0.5 – 4 Å (red) and 1 – 8 Å (blue) channels of the GOES/XRS instrument is shown in panel a. The GOES/XRS data indicate that the flare started after 06:10 UT and peaked between 06:30 and 06:35 UT. A similar trend can be seen in the 8 – 15 keV HXR flux lightcurve (blue, panel b) detected by GBM. At relatively-higher energies (15 – 20 keV; orange) there are multiple peaks between approximately 06:15 - 06:35 UT, corresponding to the impulsive and peak phases. Very little emission was detected at higher energies ( $> 20 - 50$  keV; green). Parameters of fits to the non-thermal emission in four time intervals during the impulsive phase of the flare are listed in

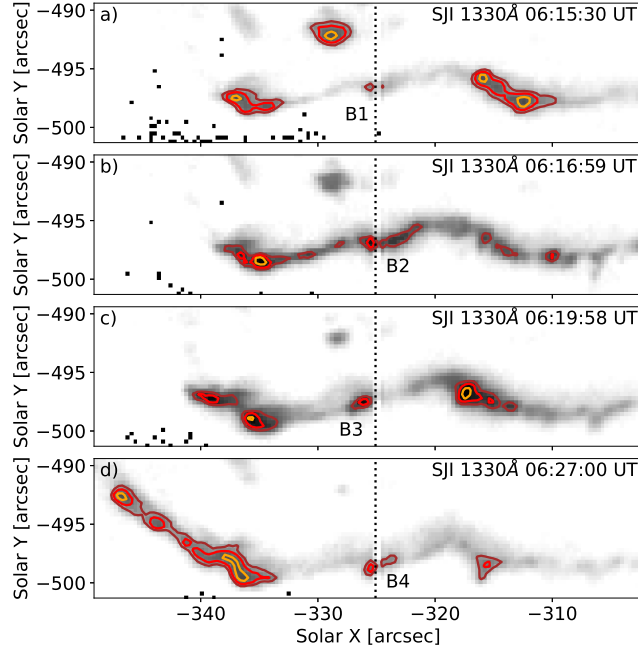


**Figure 2.** SJI 1330 Å observations of the south-western ribbon. The brown, red, and orange contours correspond to 30, 50, and 80% of the maximal intensity observed in each frame. Annotations B1 – B4 outline flare kernel brightenings that crossed the slit of IRIS (vertical dotted line). An animated version of this figure is available in the online journal. The animation covers the period between 06:15 – 06:27:30 UT and the animation duration is 17 s.

Table 1/GBM. The energy flux density was moderate, ranging between  $F = 5 \times 10^8$  and  $5 \times 10^{10}$  ergs cm<sup>2</sup> s<sup>-1</sup>, depending on the intensity threshold used for the estimation of the footpoint area (see Section 2.2). The highest energy flux density corresponds to the fit parameters obtained soon into the impulsive phase of the flare, assuming the smallest footpoint area. The lowest energy flux was measured towards the end of the impulsive phase. The other relevant fit parameters were  $E_c = 12.8 - 18.2$  keV and  $\delta \approx 3.5 - 4.1$ .

The second row of Figure 1 presents AIA 131 Å observations (panels c, d) of the flare during its impulsive phase. Flare loops started to appear soon after the flare onset and the development of the flare loop arcade continued throughout the impulsive phase. The footpoints of these flare loops are found in a pair of flare ribbons, highlighted using the red and magenta contours in panel e as observed in AIA 1600 Å. The FOV of IRIS captured a flare ribbon located in the south-west. The evolution of this ribbon during the impulsive phase of the flare is detailed in Figure 2 and its animated version. The background images correspond to SJI 1330 Å filter snapshots at 06:15:30, 06:16:59, 06:19:58, and 06:27:00 UT (panels a – d) corresponding to the start of *Fermi* integration periods during the impulsive phase. The brown, red, and orange contours outline intensity peaks corresponding to 30, 50, and 80% of the maximal intensity in each frame. The contours outline flare kernel brightenings composing the ribbon and moving along it (Lörinčík et al. 2025) as a consequence of magnetic slipping reconnection (Aulanier et al. 2006; Dudík et al. 2014). Some of the moving kernels crossed the IRIS slit, inducing enhancements visible across spectra formed in the chromosphere and the transition region. In the remainder of the manuscript we focus on brightening events, referred to as B1 – B4, characterized by the strongest spectral enhancements induced by the brightest kernels crossing the slit. While the event B1 occurred before the onset of the non-thermal event, the B2 – B4 correspond to the first three out of four periods of the *Fermi*/GBM fits.

## 4. IRIS SPECTRAL ANALYSIS

### 4.1. Properties of line profiles

Our spectral analysis was primarily focused on the Si IV 1402.77 Å, Mg II k 2796.35 Å, and C II 1334.53 Å lines. The properties of spectra were initially assessed via calculating the 0th (total intensity), 1st (centroid), and 2nd (variance) moments of the line profiles. The rest wavelengths of the Si IV and C II lines were adapted from Sandlin et al. (1986). For the Mg II line

Integration times [UT]	06:17 – 06:18	06:20 – 06:21	06:27 – 06:28	06:29 – 06:30
IRIS brightening	B2	B3	B4	-
$P_{NTE}$ [ $10^{26}$ erg $s^{-1}$ ]	3.37	2.36	1.43	1.8
$E_c$ [keV]	12.78	15.9	13.95	18.19
$\delta$	3.95	4.05	3.48	4.06
$A_{\min}$ [ $10^{16}$ cm $^2$ ]	0.76	2.56	6.34	1.63
$A_{\max}$ [ $10^{16}$ cm $^2$ ]	20.63	12.3	27.06	31.43
Min. energy flux [ $10^9$ ergs cm $^2$ s $^{-1}$ ]	1.63	1.91	0.53	0.57
Max. energy flux [ $10^9$ ergs cm $^2$ s $^{-1}$ ]	44.52	9.2	2.25	11.07

**Table 1.** Non-thermal fit parameters from *Fermi*/GBM at four instants during the impulsive phase of the flare.

we used the reference value listed in the `irisspectobs_define` routine in `SolarSoft`. The non-thermal velocity ( $v_{nt}$ ) of the Si IV line was computed using Equation (1) of [Lörinčík et al. \(2022\)](#). We assumed the square root of the variance to be equivalent to the standard deviation of the Gaussian used in the formula. The moments of the Si IV and C II lines were obtained in the wavelength range of  $\lambda_0 = \pm 0.6 \text{ \AA}$ , while a slightly larger range of  $\lambda_0 = \pm 1.0 \text{ \AA}$  was needed for the Mg II line. These wavelength ranges were determined upon manual inspection of spectra under study (Appendix A). Prior to the calculation of the moments, average continua levels were subtracted from the spectra. The Si IV spectral window sometimes exhibits the presence of weak transition region lines of ions such as O IV and S IV (e.g. [Polito et al. 2016](#)). As these lines were not present in our dataset (Appendix A), likely due to the low exposure times, they did not affect the average FUV continuum levels. On a similar note, by choosing the relatively-narrow spectral region around the Mg II k line we avoided contributions from enhanced near-continuum emission typical for quiet Sun conditions. This approach allows us to estimate the NUV continuum levels in the same way as the FUV continuum for the Si IV and C II lines. Analysis of Mg II intensities corresponding to the line’s k3 component is presented in Appendix B.

Figure 3 shows space-time maps of Si IV line spectral properties determined via the moment analysis. Since the ribbon under study only exhibited negligible separation motion ([Lörinčík et al. 2025](#)), the enhancements of spectral properties during B1 – B4 were concentrated to a narrow region along the slit between  $Y = -496''$  and  $-499''$ . The Si IV line exhibited the highest intensities during the brightening B2 imprinted by a particularly strong kernel present under the IRIS slit between  $\approx 06:17 - 06:18$  UT (see the animation accompanying Figure 2). The line was consistently redshifted (panel b, see also Appendix A), indicative of moderate downflows of  $v_D < 25 \text{ km s}^{-1}$ , a behavior typically reported during flares (e.g. [Warren et al. 2016](#); [Yu et al. 2020](#);

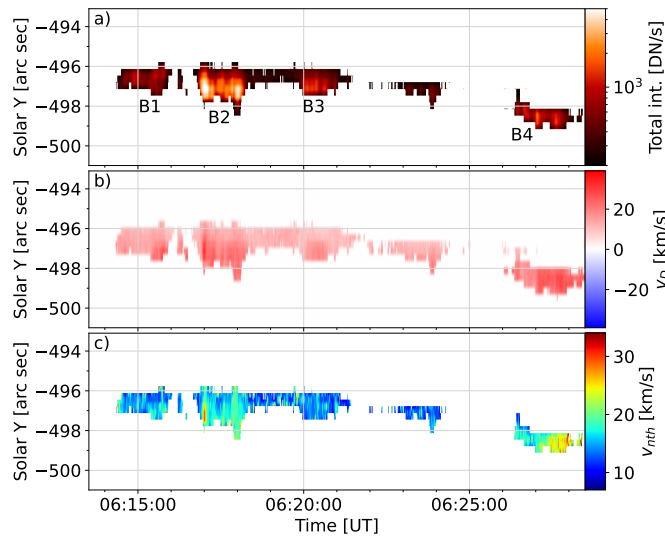


**Figure 3.** Maps of the Si IV 1402.77 Å line properties determined via the moment analysis along the slit of IRIS in the vicinity of the ribbon. Enhancements imprinted by the kernel brightenings B1 – B4 are indicated.

Wang et al. 2023). The map of the non-thermal broadening  $v_{nt}$  plotted in panel c indicates a transient episode of increase to  $v_{nt} = 30 \text{ km s}^{-1}$  at 06:17 UT during the B2. Another increase of the non-thermal broadening was observed toward the end of the time period under study. During the B4, the line broadening typically ranged between  $v_{nt} = 15 - 35 \text{ km s}^{-1}$ , compared e.g. to  $v_{nt} = 10 - 20 \text{ km s}^{-1}$  during the B3. Note that the Si IV line properties were also enhanced in the time period between 06:23 and 06:24 UT at the position  $Y \approx -497''$ , but the spectra were too noisy and we did not analyze them further.

#### 4.2. Intensity lightcurves and peaks

Figure 4 presents Si IV 1402.77 Å (grey), Mg II k 2796.35 Å (magenta) and C II 1334.53 Å (orange) lightcurves obtained via calculating the total intensity of the lines. Panels a – d show lightcurves obtained at selected positions along the slit during the brightening events B1 – B4. These lightcurves are characterized by an overall intensity increase from previous levels by a factor of few up to an order of magnitude. Several peaks can be distinguished along each lightcurve, with a duration between a few to roughly 20 s. The peaks appear to be quasi-periodic. Wavelet analysis (Torrence & Compo 1998) of the lightcurves revealed 16 – 18 s periods above  $2\sigma$  significance occurring in short episodes. While some peaks appeared repeatedly one after another, the lightcurves also exhibited short periods where no peaks were present (see e.g.  $t = 50 \text{ s}$  in panel a or  $t = 40 \text{ s}$  in panel d). Note that intensity peaks with characteristics similar to those in the spectra were also observed in SJI 1330 Å data in flare ribbon pixels adjacent to the slit of IRIS (not shown). This suggests that the intensity peaks were driven by the passage of slipping flare kernels under the slit (see Section 6).

To study the timings and characteristics of the individual peaks, the lightcurves were segmented in order to isolate time periods when the peaks occurred in each ion separately. The peak time intervals are designated using the horizontal colored lines above the lightcurves in the same figure. Manually-identified onset time of a particular peak, referred to as the ‘left base’, is indicated using the colored triangles ( $\triangleright$ ) above the lightcurves. The time when the intensity drops before rising again (or the end of the lightcurve) is referred to as the ‘right base’ ( $\triangleleft$ ). The left and right bases were used to calculate the amplitude (in DN/s) of each peak as

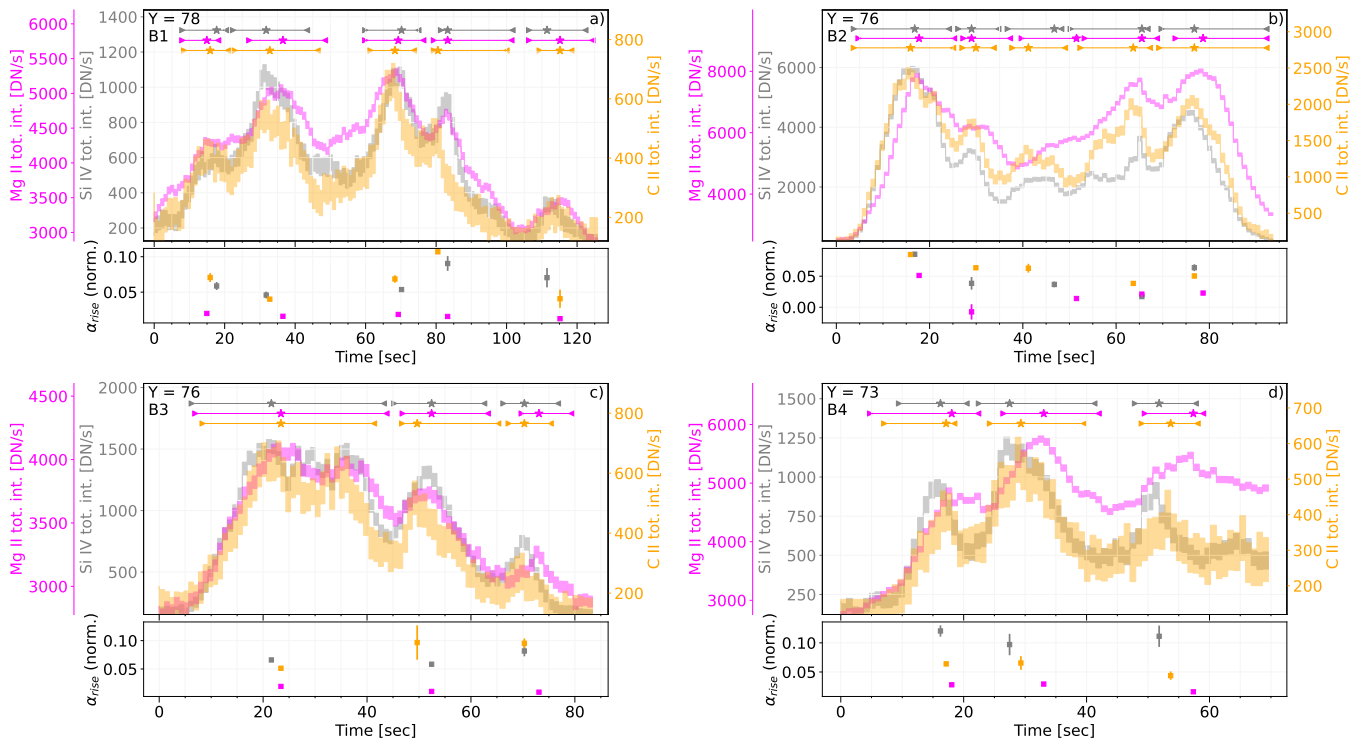


**Figure 4.** Si IV 1402 Å (grey), Mg II 2796.35 Å (magenta), and C II 1334.53 Å (orange) line lightcurves during the B1 – B4 brightening events in the ribbon observed by IRIS. The colored horizontal bars above the lightcurves indicate manually-identified peak intervals. The triangle symbols are the left and right bases (peak onset and end times), while the stars designate the maximum of each peak. The bottom part of each panel indicates the slopes of each peak after normalization.

$$I_{\max} - \frac{|I_{\text{left base}} + I_{\text{right base}}|}{2}. \quad (1)$$

When designating the peak time intervals, we only focused on peaks (and troughs separating them) common to all spectra. For instance, in Figure 4a we identified five major peaks across the three lightcurves. A distinct behavior is apparent in the time interval between 35 – 70 seconds in Figure 4b. During this period, the Si IV and C II lines exhibited three clear peaks, while only one strong ( $t = 60$  s) and one very weak ( $t = 45$  s) peak are visible in the Mg II line lightcurve. In such cases, the peak bases were adapted from the lightcurve exhibiting fewer peaks. Despite our efforts in the precise determination of the peak intervals, certain challenges arose, particularly in C II lightcurves with higher noise level or Mg II k3 lightcurves (Appendix B). Peaks visible in the lightcurves were also occasionally separated by flat plateau rather than deep troughs, complicating the selection of the interval boundaries. In order to mitigate the human bias in designating the peaks and their bases, the selection was also performed via an automatic routine. This process, described in Appendix C, confirmed the results of our manual analysis, however at the expense of using data with a higher grade of smoothing. In the remainder of the manuscript we thus focus on peaks determined manually.

The most intriguing characteristic of the lightcurves is that the times when the individual peaks reach maxima differ across the three ions. These instants are for clarity indicated using the star symbols along the respective peak intervals above the lightcurves in Figure 4. The Si IV 1402.77 Å line peaks (grey stars) and C II line peaks (orange stars) were typically occurring before those visible along the Mg II 2796.35 Å lightcurves (magenta stars). The horizontal separation between the stars is a measure of the delay between the line peaks, and is typically of the order of a few seconds or less. To our knowledge, delays between the line emission formed in different regions of the lower solar atmosphere at these timescales have not yet been reported. This is the key result of our study and the observable we focus on in the remainder of this manuscript.

The delays between the peak maxima alone do not account for the overall time evolution of the peaks. While some of the peaks across the ions reach maxima simultaneously or close in time, they can exhibit time evolution characterized by distinct peak widths, asymmetry, or steepness across the three lightcurves. Here we determined the peak steepness by fitting the ascending segment of every peak, bounded by the left base and peak maximum, with a linear function weighted by intensity uncertainties via the `statsmodels` Python module. Because the peak bases often correspond to different instants across the three ions due to the distinct peak time evolution, the endpoints of linear fits were chosen to be ion-specific. To account for the differences of peak amplitudes across the lightcurves, we normalized the slopes of peak rise  $\alpha_{\text{rise}}$  by peak strengths.  $\alpha_{\text{rise}}$  of every peak is indicated at the bottom of each panel in Figure 4, with the same color-coding as used for the lightcurves above. The slopes of the Si IV and C II intensity peaks are usually close one to another and higher than the ascending slopes of the Mg II peaks. One exception occurs (at  $t \sim 65$  s in source B2), during the time period exhibiting a different number of peaks across the ions. The individual Si IV peaks at  $t = 50 - 70$  s are steeper than the single Mg II peak in this time window, but when merged into a single peak interval (see above) the ascending slope appears less steep. The C II intensity evolution is generally similar to that of the Si IV line, with the peaks being stronger and troughs separating them deeper compared to those along the Mg II k lightcurves. Because of the similarity between the Si IV and C II intensity evolution and the higher noise levels in the C II lightcurves, hampering the peak determination therein, we opted to further analyze the delays between the transition region Si IV and chromospheric Mg II k line emission only.

#### 4.3. Quantifying delays between Mg II and Si IV line emission

The delays between the maxima of the individual Si IV and Mg II intensity peaks are plotted in Figure 5 as a function of time. Panel a shows the delays between the peaks in the lightcurves produced via the total line intensities (Figure 4). The time is indicated on the horizontal axis in seconds after the start of the observations and spans most of the impulsive phase of the flare. Positive delays (vertical axis) imply that the Si IV intensity peaks precede those visible in the Mg II line and vice versa. The size of the symbols is given by the amplitude of the Si IV peaks whose delay the symbol indicates; the larger the symbol, the larger the peak amplitude. Finally, the grey strip at  $y = 0$  corresponds to  $\pm\Delta_t/2$ , where  $\Delta_t \approx 0.92$  is the cadence of the spectral observations.

Si IV intensity peaks occurred before those in the Mg II line the majority of the time, with 11 out of 16 measurements (69%) exhibiting a positive delay. The longest delays are  $\approx 6$  s long, whereas 2 out of the 11 positive delays are below  $\Delta_t$ . The mean of the measured delays  $\delta_t$  was determined as  $1.8 \pm 0.6$  s with a standard deviation  $\sigma$  of 2.5 s. The mean positive delay is  $\delta_t = 3.1 \pm 0.6$  s with  $\sigma = 1.9$  s. The green dotted line plotted in Figure 5 represents linear fit to the delays, with Si IV peak amplitudes used as weights. Despite the low number of the datapoints, the trend indicated by the linear fit is suggestive of an overall increase of the emission delays as the flare was progressing in the region under study. The Si IV peak maxima were occurring consistently before their Mg II k counterparts after  $t \approx 2100$  s in Figure 5. The last three datapoints plotted in Figure 5 correspond to the B4 at the end of the impulsive phase of the flare.

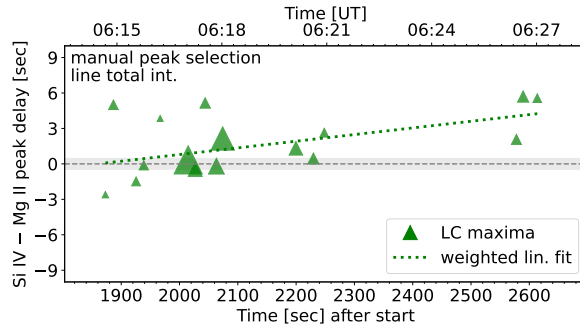


**Figure 5.** Delays between the maxima of Si IV and Mg II k line intensity peaks inferred from the total line intensities as a function of time during the flare. The peaks whose maxima were used for the delay calculation were selected manually. The size of the symbols is given by the amplitude of Si IV peaks. The dotted line represents linear fit to data weighted by the peak amplitude. The grey horizontal strip at  $t = 0$  s corresponds to  $\pm\Delta_t/2$ .

Delays between the Si IV and Mg II k3 intensity maxima are briefly discussed in Appendix B. Analysis of line emission delays inferred via peak cross-correlations and peak centroids is presented in Appendix D. We find that, while the relative delays between the line emission can vary when the peak time evolution is accounted for, the results are generally consistent with the delays inferred from peak maxima.

The IRIS spectral analysis of the newly-discovered delays between the chromospheric and transition region emission can be summarized in few key points:

1. The transition region emission intensity peaks typically precede the emission originating in the chromosphere (Si IV precedes Mg II);
2. The typical delay time is up to  $\approx 6$  seconds;
3. There is seemingly an increase of the delay toward the end of the impulsive phase.

Even though the peak delays can also be discerned in slit positions adjacent to those presented in Figure 4, the high-cadence sit-and-stare IRIS observations cannot address the spatial distribution of the delays in the full length of the ribbon structure. These outcomes are only inferred from the four brightening events B1 – B4 in the ribbon portion coincident with the IRIS slit, and they might not be representative of the general flare behavior (see Section 6). On the other hand, these results hold irrespective of the method used for detection of intensity peaks and peak intervals (Appendix C) and determination of delays (Appendix D). The robustness of this result is underlined by the fact that the delays are evident in both level-2 data free of any post-processing (not shown), as well as lightcurves with various degrees of smoothing (Figure 4, Appendix Figure 3). The short delay times are the likely reason why they have not been reported in previous spectroscopic observations, often limited by lower time resolution.

## 5. INTERPRETING THE OBSERVED DELAYS USING RADYN SIMULATIONS

### 5.1. RADYN flare models

Motivated by the new observations of delays between transition region Si IV and chromospheric Mg II emission, one-dimensional (1D) field-aligned flare simulations were performed, in which the agent of energy transport through the solar atmosphere varied. Our aim was to determine what these observations tell us about flare energetics and about the energy propagation through flaring atmospheres, that leads to the formation of the observed delays. For this we utilized the RADYN code (Carlsson & Stein 1992, 1995, 1997; Allred et al. 2005, 2015), which is a powerful tool to study the radiative and hydrodynamic response of the solar atmosphere to flares, from the photosphere through the corona. RADYN solves the coupled, non-linear equations of hydrodynamics, non-LTE radiative transfer and non-equilibrium atomic level populations, on a one-dimensional (1D) adaptive grid, allowing for resolution of shocks and gradients in the chromosphere and the transition region. Optically thick radiation transfer is included for H, Ca, and He. We subjected different pre-flare atmospheres to electron beam (EB), thermal conduction (TC), TC + EB (hybrid; H), and Alfvén wave (AW) heating.

Upon estimating the lengths of flare loops connecting the two ribbons (Figure 1c – d) we assumed a half-loop length of 50 Mm. Flare energy was injected at a constant rate for  $\tau_{inj} = 10$  s. This duration was estimated from the intensity peaks along the IRIS

intensity lightcurves (Section 4.2). We assumed four different initial loop atmospheres: (1) an atmosphere in radiative equilibrium ('RE', e.g. Allred et al. 2015) with no ad-hoc chromospheric heating at coronal apex  $T = 1$  MK, (2) a similar setup but with coronal apex  $T = 3$  MK, (3) an atmosphere with initial ad-hoc chromospheric heating to create an extended chromospheric plateau (referred to as 'plage'-like atmosphere, following Carlsson et al. 2015; Polito et al. 2018), with coronal apex  $T = 1$  MK, and (4) that same plage chromosphere but with coronal apex  $T = 3$  MK. Initial loop apex temperatures of  $T = 1, 3$  MK are based on active region observations and commonly used to model flare emission (e.g. Kašparová et al. 2009; Allred et al. 2015; Carlsson et al. 2023).

The properties of the EB heating were constrained by parameters of fits to non-thermal components of *Fermi*/GBM spectra (Table 1). As discussed in Section 2.2, the inferred energy flux densities injected to the RADYN simulations were constrained via two sets of footpoint area measurements,  $A_{\min}$  &  $A_{\max}$ . The corresponding flux densities  $F$  were:  $[1 \times 10^9, 5 \times 10^9, 1 \times 10^{10}, 5 \times 10^{10}] \text{ erg cm}^{-2} \text{ s}^{-1}$ . The low-energy cutoff was fixed at  $E_c = 15$  keV, and the spectral index at  $\delta = 4$ , to approximate the values found in the *Fermi*/GBM analysis. The lowest observationally-constrained value of  $F = 5 \times 10^8 \text{ erg cm}^{-2} \text{ s}^{-1}$  (see  $A_{\max}$  during the B4, Table 1) produced EB model flare atmospheres that did not contain measurable Si IV 1402.77 Å emission, so they were excluded from the analysis. Indeed, according to the models of Polito et al. (2023a); Kerr et al. (2024b), such low values of energy flux densities are closer to what would be expected to appear in the ribbon fronts, rather than the bright kernels that we study here. The *Fermi*/GBM inspired simulations were supplemented by experiments with  $F = 1 \times 10^9 \text{ erg cm}^{-2} \text{ s}^{-1}$ ,  $E_c = 5$  keV, and  $\delta = 4$ , for each of the four pre-flare atmospheres. These models were tested to account for the possibility that the non-thermal electron distribution had an  $E_c = 5$  keV, below the sensitivity threshold of *Fermi*/GBM.

Further, we ran flare models assuming purely *in-situ* heating in the corona and consequent energy propagation to the lower atmosphere through a thermal conduction front (here referred to as "TC models"). Similar to previous studies (e.g. Testa et al. 2014; Polito et al. 2018), we assume a volumetric heating rate ( $\text{ergs s}^{-1} \text{ cm}^{-3}$ ) distributed over a certain region along the loop. We use the same values of total energy flux density energy as that of the EB simulations, but spread over the coronal portion of the loops. For all TC models, the heating is distributed between the loop apex and  $3 \times 10^8$  cm (at the boundary between the corona and the top of the TR). To aid comparison with the EB models, we list the TC models based on energy flux rather than volumetric heating rate. Some of the simulations with the largest energy fluxes ( $F = [5 \times 10^9, 5 \times 10^{10}] \text{ erg cm}^{-2} \text{ s}^{-1}$ ) were excluded from our analysis, as they caused the atmosphere to reach temperatures above 100 MK that are unrealistic for the relatively small C-class flare analyzed here. The excluded runs were replaced with simulations with slightly lower flux ( $F = [2.5 \times 10^9, 2.5 \times 10^{10}] \text{ erg cm}^{-2} \text{ s}^{-1}$ ).

We have also ran two test cases where the heating was equally distributed between the TC *in-situ* heating and EB energy models. We have done so for two energy fluxes,  $F = [5 \times 10^9, 5 \times 10^{10}] \text{ erg cm}^{-2} \text{ s}^{-1}$ , and called these models "Hybrid (H)".

The last energy transport mechanism that we explored was downward propagating Alfvén waves (Emslie & Sturrock 1982; Fletcher & Hudson 2008; Haerendel 2009; Russell & Fletcher 2013; Reep & Russell 2016; Kerr et al. 2016; Reep et al. 2018). The implementation of AW in RADYN flare simulations of Kerr et al. (2016) was updated to include the wave travel time in the computation. This closely follows the approach of Reep et al. (2018), such that the wave moves at the local Alfvén speed as it travels down the loop. A complete description of updates to AW energy transport in RADYN will be presented in a forthcoming manuscript (Kerr et al. 2025). To model energy transport via AW we impose a magnetic field stratification for the purpose of calculating the Alfvén speed. It does not vary in time. This was set to  $B = 1500$  G in the photosphere, and  $B \sim 500$  G in the low corona, evolving with pressure according to Eq. 10 of Kerr et al. (2016). Photospheric fields of similar strengths can be found in the strong-field regions of the NOAA AR13107. While Lörinčík et al. (2025) suggested that the environment where the flare occurred was disperse with potentially weaker coronal fields, these field strengths were chosen to provide a reasonable upper constraint on  $B_{\text{LOS}}$  consistent with the HMI observations. Injected AWs had frequency = 5 Hz and perpendicular wave number at loop apex  $k_{x,a} = 5 \times 10^{-4} \text{ cm}^{-1}$  (varying linearly with magnetic field through the loop). The Poynting flux corresponds to that of the EB models constrained by the HXR fitting, although here we only selected three example models  $S = [5 \times 10^8, 1 \times 10^9, 1 \times 10^{10}] \text{ erg s}^{-1} \text{ cm}^{-2}$  for a detailed study. The particular values of the frequency and wavenumber were chosen because they produce a significant increase of Si IV intensity, which is needed to explain the peaks in intensity. A broader parameter study of the Si IV response to wave heating has been conducted by Kerr et al. (2025). As with the EB and TC experiments, energy was injected for a duration of 10 s. Unlike the EB experiments, in these AW experiments the energy injected in the corona takes time to reach the lower atmosphere, where energy losses takes place due to resistive damping, including ambipolar effects.

Model	$F$ [ergs cm <sup>2</sup> s <sup>-1</sup> ]	$T_{\text{init}}$ [MK]	Init. atm.	Delays reproduced?
EB1	1F09	1	RE	×
EB1p	1F09	1	plage	×
EB2	1F09	3	RE	×
EB2p	1F09	3	plage	×
EB3	5F09	1	RE	×
EB3p	5F09	1	plage	×
EB4	5F09	3	RE	×
EB4p	5F09	3	plage	×
EB5	1F10	1	RE	×
EB5p	1F10	1	plage	×
EB6	1F10	3	RE	×
EB6p	1F10	3	plage	×
EB7	5F10	1	RE	✓
EB7p	5F10	1	plage	✓
EB8	5F10	3	RE	✓
EB8p	5F10	3	plage	✓
EB9*	1F09	1	RE	✓
EB9p*	1F09	1	plage	✓
H1	5F09	3	RE	×
H2	5F10	3	RE	✓
TC1	1F09	1	RE	×
TC2	2.5F09	1	RE	×
TC3	5F09	3	RE	×
TC4	1F10	3	RE	×
TC5	2.5F10	3	RE	×
AW1	5F08	3	RE	✓
AW2	1F09	3	RE	✓
AW3	1F10	3	RE	×

**Table 2.** List of electron beam (‘EB’), hybrid (‘H’), thermal conduction (‘TC’), and Alfvén wave (‘AW’) heating models analyzed in this study. The columns of the table list the varying model parameters. The rightmost column indicates whether the model reproduces the observed delays between the Si IV and Mg II peaks. EB simulations assume  $\delta = 4$  and  $E_c = 15$  keV.

\* $E_c = 5$  keV models.

## 5.2. Synthetic lightcurves

Synthetic Si IV 1402.77 Å emission was produced assuming equilibrium conditions and atomic data from the CHIANTI version 10 model (Dere et al. 1997; Del Zanna et al. 2021) at a timestep of 0.5 s (see Polito et al. 2018, for details). To produce synthetic Mg II 2796.35 Å emission, the radiation transfer code RH15D (Uitenbroek 2001; Pereira & Uitenbroek 2015) was used, taking account of partial redistribution effects. The spectra were synthesized assuming microturbulence of  $v_{\text{turb}} = 7$  km s<sup>-1</sup> and a filling factor of one. For further details on the experiment setup, including conversion to IRIS count rates, we refer the reader to Polito et al. (2023a) and Kerr et al. (2024a). To facilitate the comparison between the observations and models, the properties of the synthetic profiles were obtained via the moment analysis using the same wavelength intervals as those used for the observations (Section 4.1).

Figure 6 presents Si IV 1402.77 Å (grey) and Mg II 2796.35 Å (magenta) synthetic lightcurves corresponding to each line’s total intensity. The dotted sections along certain Mg II lightcurves are interpolated values, where the RH15D code failed to converge to a solution. The lightcurves were normalized to facilitate comparison with the observations. Observed and modeled spectral characteristics such as total intensities, Doppler shifts, and line broadening are compared in Section 5.3.

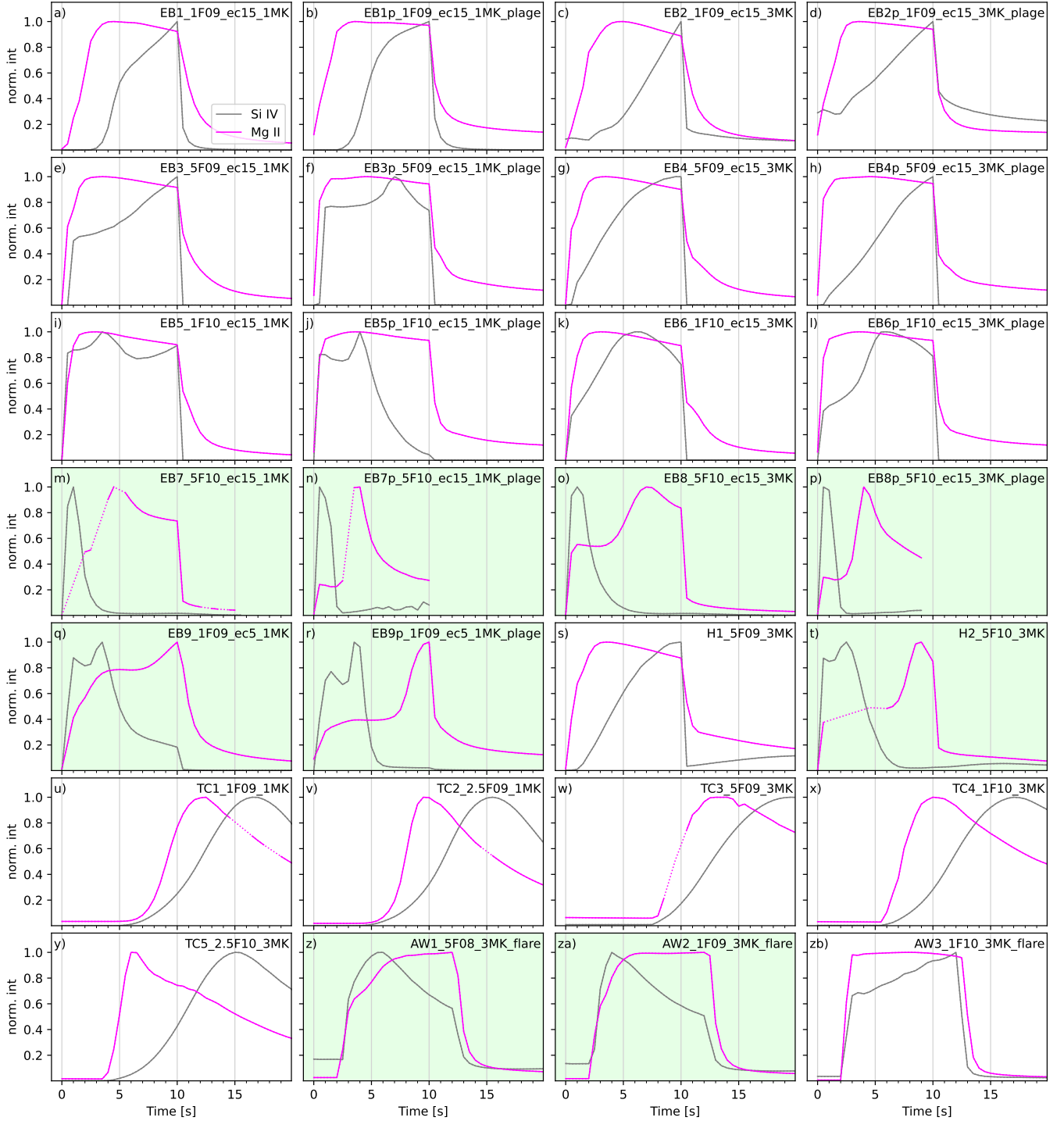


**Figure 6.** Lightcurves of Si IV 1402.77 Å (grey) and Mg II 2796.35 Å (magenta) synthesized from our grid of RADYN simulations. Panels a – r present curves in electron-beam heated atmospheres, panels s, t were obtained in hybrid simulations, panels u – y correspond to thermal conduction-heated atmospheres, and panels z – zb to simulations with the Alfvén wave heating. Dotted sections along the lightcurves represent interpolated values (where applicable). Green semi-transparent background was used to highlight lightcurves that replicate the observed delays.

In contrast to the observations, the modeled Si IV and Mg II lightcurves usually consisted of a single peak only, a key difference caused by the properties of the heating profile. The lightcurves obtained in the EB (panels a – r) and H (panels s & t) models are characterized by a steep increase of the intensity of both or either of the two lines immediately after the start of the heating. More

gentle intensity increases are characteristic for the TC model lightcurves (Figure 6 u – y), while the AW heating (z – zb) again results in a steep intensity increase (for the chosen wave parameters), albeit delayed from the simulation start by 2 – 3 s due to the wave’s travel at the local Alfvén speed. The intensity decrease begins at  $t = 10$  s, right after the heating is switched off, in the EB and H models (panels a – t) and again slightly later in the AW models (z – zb). In the EB and H models, the Si IV emission is only at a level that would be detectable by IRIS during the heating period. Mg II k lightcurves decline more gradually compared to Si IV.

The delays between the modeled Si IV and Mg II emission and their comparison to the observations are visualized in Figure 7. The histogram presents the distribution of the observed delays corresponding to the total intensities. The grey strip at 0 s corresponds to  $\pm\Delta_t/2$ . The symbols above the histogram indicate the delays between the maxima of the synthetic lightcurves. Different symbol styles were used to distinguish between the models (see the legend of Figure 7 for further reference). Of the 28 runs studied here, 9 simulations (6 different heating models, with some that worked for both pre-flare atmospheres) produced a delay of Mg II lightcurve maxima relative to Si IV, also highlighted using the green semi-transparent background in Figure 6. This occurred in:

- the high-flux ( $F = 5 \times 10^{10}$  ergs cm<sup>2</sup> s<sup>-1</sup>) EB7 – EB8p models (Figure 6 m – p);
- the low flux, small  $E_c$  ( $F = 1 \times 10^9$  ergs cm<sup>2</sup> s<sup>-1</sup>,  $E_c = 5$  keV) EB9 and EB9p models (Figure 6 q & r);
- the high-flux H2 model (Figure 6 t); and
- the AW1 & AW2 models (Figure 6 z & za).

The delays obtained via cross-correlating the lightcurves and calculating peak centroids are discussed in Appendix D.

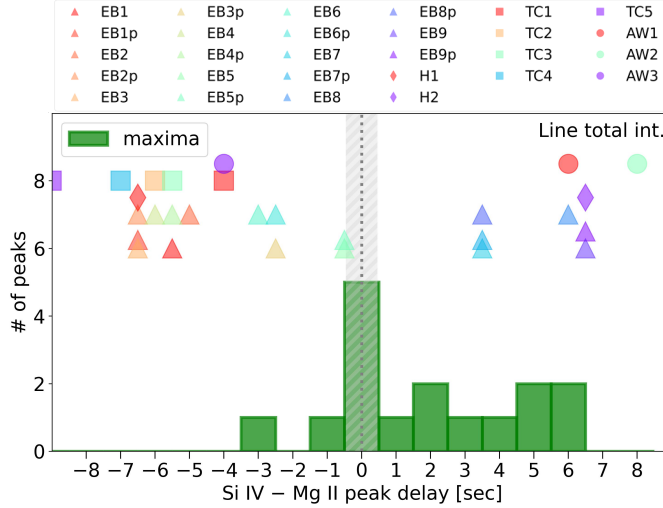


**Figure 7.** Histograms depicting the distribution of the observed delays inferred from the total Si IV and Mg II line intensities. The symbols above the histograms correspond to the delays between synthetic lightcurves, and are the same for both panels. Different symbol styles and colors were used to distinguish between the models (see the legend above the figure). The hatched grey strip at  $t = 0$  s corresponds to  $\pm\Delta_t/2$ .

### 5.3. Comparison of observed and modeled spectral properties

The time evolution of the spectral properties of the Si IV 1402.77 Å and Mg II 2796.35 Å lines synthesized in the models which reproduce the observed delays is presented in Figure 8. Panels a1 & a2 show the total line intensities, panels b1 & b2 depict the Doppler velocities  $v_D$ , and panels c1 & c2 detail the evolution of the broadening, expressed in terms of the non-thermal velocity  $v_{nt}$  for Si IV. The black horizontal lines correspond to the average of the quantities observed during the brightening events B1 – B4. Since reproducing some of the observed Mg II line properties in flare models can be difficult (see e.g. Rubio da Costa & Kleint 2017; Polito et al. 2023a; Kerr 2023; Kerr et al. 2024a, and references therein), the following analysis is mostly focused on the Si IV line.

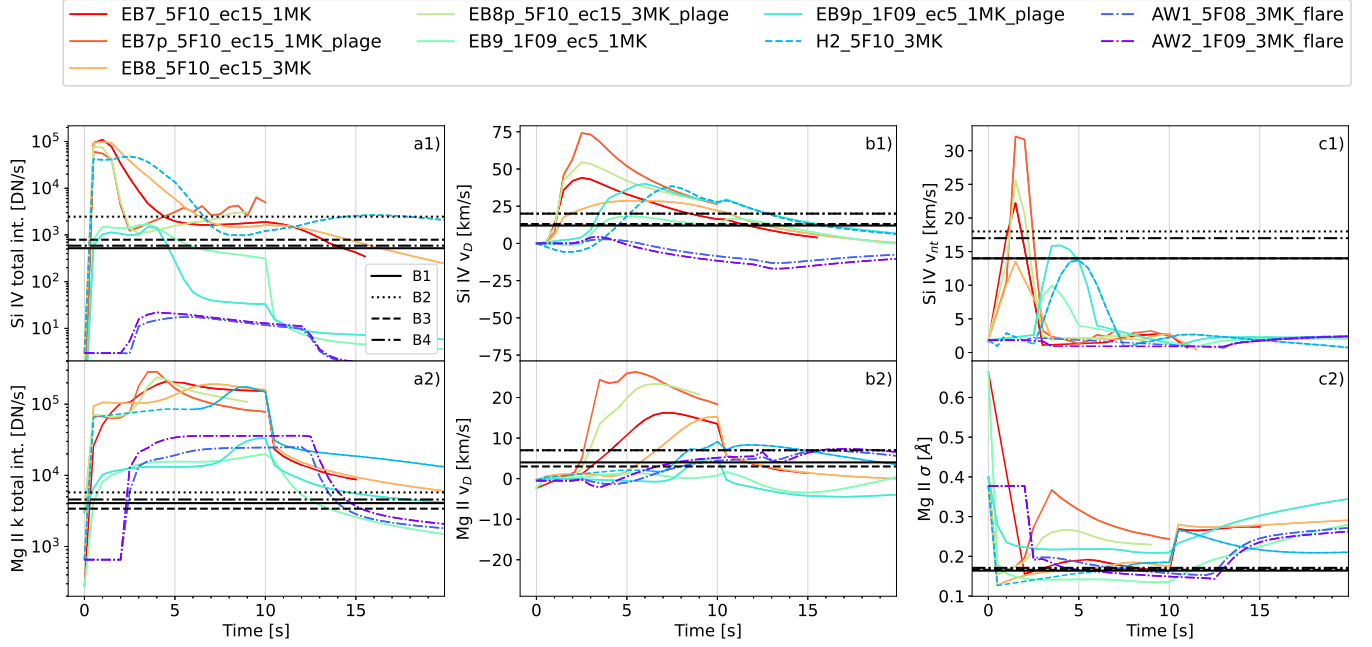


**Figure 8.** Evolution of the total intensity (panel a), the Doppler velocity (panel b), and the broadening ( $v_{nt}$ ,  $\sigma$ ; panel c) of the Si IV 1402.77 Å (top) and Mg II 2796.35 Å (bottom) spectra synthesized in the models which reproduce the observed delays. The color-coding and different linestyles distinguish between the models. The black horizontal lines correspond to the observed values averaged during the B1 – B4 events.

The line intensities observed during the B1 – B4 were typically of the order of  $10^2 - 10^3$  DN s $^{-1}$  for the Si IV line and  $10^3$  DN s $^{-1}$  for Mg II. As seen in Figure 8a1, a2, the synthetic intensities rarely align with the observations, in some cases exceeding the observed ones by up to two orders of magnitude, particularly for the Mg II line. The difference between the modeled and observed intensities can be attributed to using an ad-hoc filling factor and possible multithreaded structure of loops. These factors, on the other hand, should not affect the ratios of the synthetic intensities. The observed ratios between the Mg II and Si IV line intensities averaged during the B1 – B4 range roughly between 2 – 8. Similar synthetic ratios can be found in the EB7 & 7p, EB8 & 8p (red  $\rightarrow$  gold solid lines) and EB9 (green) models in the first  $\approx 4$  s after the start of the heating. These ratios later grow to  $\approx 10^1 - 10^2$ , values also found in the H2 model (blue dashed line). The ratios obtained in the EB9p model (turquoise) are also fairly close, around 10 in the same time period. The Mg II vs. Si IV ratio in the AW1 & 2 runs is of the order of  $10^3$ , far from the observed values.

The Si IV profiles synthesized in the EB and H models are redshifted and the magnitude of the Doppler shifts is comparable to the observations (Figure 8b1). The high-flux plage EB7p and EB8p models (light-red and gold solid lines) show redshifts in the excess of  $50$  km s $^{-1}$ , roughly factor of 2 higher than the observations. The AW models reproduce mild ( $< 20$  km s $^{-1}$ ) Si IV blueshifts, particularly towards the end of the heating period, which do not align with the observations (c.f. blue curves and black horizontal lines). These blueshifts are preceded by very weak ( $v_D < 5$  km s $^{-1}$ ) and brief redshifts  $\sim 2 - 4$  s after the start of the simulation during the rise of the Si IV intensity. All of the models under consideration reproduce mild Mg II redshifts consistent with the observations (Figure 8b2).

The last spectral property constraining our models is the line broadening. The Si IV non-thermal velocity (Figure 8c1) exhibits a transient increase to  $v_{nt} \sim 30$  km s $^{-1}$  after the start of the heating in the high-flux EB7 & 8 models, whereas the  $E_c = 5$  keV EB9, 9p models as well as the H2 model exhibit a milder increase to  $\sim 15$  km s $^{-1}$   $\sim 3$  s into the heating. The modeled  $v_{nt}$  generally correspond well to the observations, indicative of  $v_{nt}$  ranging between  $10 - 20$  km s $^{-1}$ . The AW models do not exhibit  $v_{nt}$  increase in the Si IV line, although we note that we have not included any potential non-thermal broadening due to the Alfvén wave itself. The proxy on the Mg II line broadening obtained from the 2nd moment is comparable to the observations. The standard deviation  $\sigma$  drops from the pre-flare levels to  $\sigma \sim 0.15 - 0.2$  Å during the heating period in all but the EB7p and EB8p models. Converted to the Gaussian FWHM of  $\sim 0.35 - 0.47$  Å, this range is consistent with the widths of the observed profiles (Appendix A). We emphasize that, in contrast to the observed typically single-peaked Mg II profiles, the synthetic spectra were usually double-peaked and therefore this should be taken as a quantitative, and not fully accurate, comparison.

To summarize this comparison, the high-flux ( $F = 5 \times 10^{10}$  ergs cm<sup>2</sup> s<sup>-1</sup>) EB7 & EB8 simulations produce synthetic spectra that are generally consistent with the observations. In addition to reproducing the observed delays, the properties of spectra synthesized in the  $E_c = 5$  keV EB9, 9p models show relative intensities, widths, and Doppler shifts comparable to the observations. Two out of three AW models included in our study reproduce the observed delays, but the synthetic Si IV spectra are blueshifted and the relative intensities do not align with the observations (see also Section 6).

#### 5.4. Comparing the chromospheric and transition region electron density evolution

Next, we aim to investigate the differences between physical conditions in example models which do and do not reproduce the observed delays between the Si IV 1402.77 Å and Mg II 2796.35 Å line emission. In the dataset under study, the Si IV line spectra were only observed in the flare ribbon during the relatively-short brightening events B1 – B4. Mg II line spectra, on the other hand, were visible even outside of the ribbon as well as before the flare onset. The visibility and the increase of intensity of the Si IV line at such short (0.3 s) exposure times is thus contingent upon ongoing heating, which is confirmed by the modeling (Figure 6). If we consider the Si IV line to be optically thin, its intensity is proportional to the square of the electron number density  $N_e$ . This is a reasonable assumption given the magnitude of the non-thermal electron flux detected by *Fermi*/GBM and the Gaussian-like line profiles with no traces of absorption features (see Appendix Figure 1, left), though possible opacity effects cannot be entirely excluded (see details in Kerr et al. 2019).

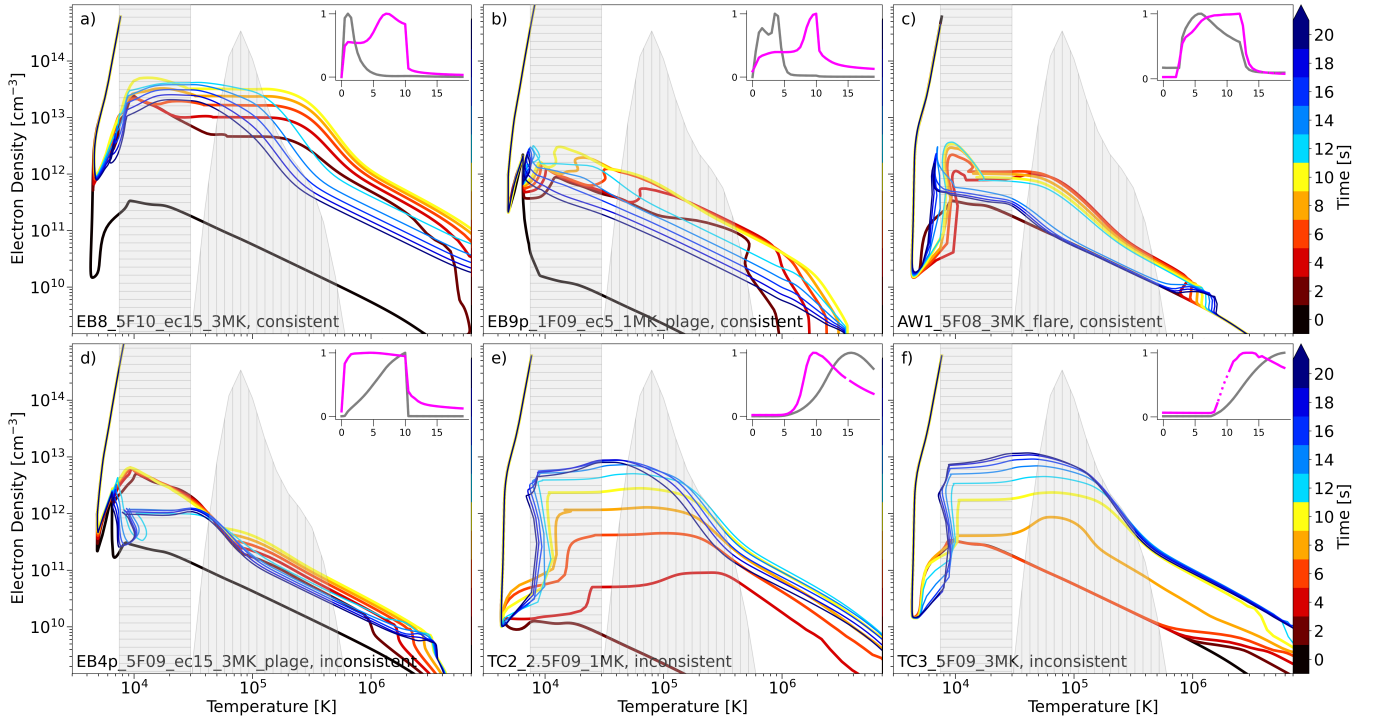


**Figure 9.** Electron density as a function of temperature in selected models that are consistent (top row) and inconsistent (bottom row) with observed delays. Color represents simulation time, with curves shown at 2 s increments. The pre-flare is the black curve. The heating period (brown → yellow thick curves) and the cooling period (cyan → dark blue thin curves) are both included. The hatched gray semi-transparent areas in the background indicate the rough formation region of the Mg II 2796.35 Å line (horizontal hatches) and the normalized contribution function of the Si IV 1402.77 Å line (vertical hatches). Inserts in the top-right corner show the Si IV (gray) and Mg II (magenta) lightcurves synthesized in each model. Details of heating parameters are provided in the lower left corners.

As a proxy for probing  $N_e$  in the formation region of each line we explored the temporal variation of  $N_e$  as a function of the gas temperature  $T$ . The resulting curves are shown in Figure 9 at a 2 s cadence, where color represents time during the simulation (black is the pre-flare). The ‘warm’ color palette (brown → yellow thick curves) corresponds to the heating period, whereas the ‘cold’ colors (cyan → dark blue thin curves) designate the cooling. On each panel, the gray semi-transparent area with vertical hatches is the normalized contribution function of the Si IV, assuming  $\log(N_e [\text{cm}^{-3}]) = 12$ . The formation region of the Mg II k line cannot simply be outlined in the  $N_e$  vs.  $T$  parameter space as it varies with time due to NLTE radiation transfer effects. For a crude estimation of the line’s formation region we plot a gray semi-transparent area with horizontal hatches, corresponding to

$7.5 \times 10^3 - 30 \times 10^3$  K. This area outlines the range of radiation temperatures where most of the Mg II k line emission is formed (Kerr et al. 2024a). The heating parameters as well as whether the model is consistent with the observations are indicated in the lower-left corner of each panel. The inserts in the upper-right corner show the normalized lightcurves synthesized in the selected atmospheres, the same as those in Figure 6.

The top row of Figure 9 (panels a – c) contains selected models consistent with the observations. The EB8 and EB9p models (panel a, b) are characterized by a rapid increase of  $N_e$  over more than 2 orders of magnitude in both the chromospheric and transition region line formation regions. This rapid  $N_e$  increase causes a commensurately rapid intensity increase of both lines. In the EB8 model, the transition region  $N_e$  continues to increase over the following  $\sim 8$  s (brown  $\rightarrow$  yellow curves, panel a), although the Si IV lightcurve peaks within  $\approx 2$  s after the heating onset. The gradual  $N_e$  increase in the transition region occurs at  $\sim 4 - 6$  s (red curves, panel b) and the Si IV lightcurve reaches maximum at  $t = 4$  s in the EB9p model. The  $N_e$  increase subsequently progresses into the upper chromosphere, reached at  $t = 6$  and  $8$  s in the EB8 and EB9p models, respectively. These instants are close in time to the Mg II lightcurve maxima. The  $N_e$  increase in the AW1 model (panel c) is delayed by  $t \sim 4$  s from the injection of the wave into the loop. The transition region  $N_e$  growth in that model is more significant and abrupt compared to the more gradual growth in the chromosphere, resulting in the Mg II lightcurve trailing the Si IV one.

Model atmospheres that do not reproduce the observed delays are plotted in the bottom row of Figure 9. The  $N_e$  evolution in the EB4p model (panel d), is characterized by rapid and significant density increase in the chromosphere immediately after the onset of the heating, remaining nearly constant for the first 10 s, of the simulation. A consequence of this density increase is the near-instantaneous growth of the Mg II line intensity, reaching maximum within the first two seconds after the heating onset. This Mg II behaviour occurs in all of the  $F = [5 \times 10^9, 1 \times 10^{10}]$  ergs  $\text{cm}^{-2} \text{s}^{-1}$  EB models as well as the  $F = 5 \times 10^9$  H1 model. The  $N_e$  increase in the transition region, and the subsequent Si IV intensity growth is more gradual in those models, peaking at  $t = 10$  s.

The TC2 model (panel e) shows a jump in the transition region  $N_e$  from the pre-flare  $N_e \lesssim 10^9 \text{ cm}^{-3}$  by roughly two orders of magnitude at  $t \sim 4$  s. This initial jump is also evident in the upper chromosphere, albeit less pronounced. The  $N_e$  increase propagates from the upper to the lower chromosphere as the time goes by. After  $t = 6$  s,  $N_e$  increases in both the chromosphere and the transition region at roughly the same rate, at which the intensities of both lines start to rise. Non-normalized lightcurves (not shown) indicate that the Si IV line becomes observable only when the  $N_e$  in the transition region exceeds the order of  $10^{11} \text{ cm}^{-3}$ . On the other hand, the continuing chromospheric  $N_e$  increase contributes to the Mg II line intensity observed at  $\approx 200 \text{ DN s}^{-1}$  as soon as the heating sets on. The Mg II emission shows a steeper rise compared to Si IV and peaks when the  $N_e$  in the chromosphere exceeds the order of  $10^{12} \text{ cm}^{-3}$  at  $t \sim 10$  s (yellow). The Si IV emission continues to progressively increase together with the transition region  $N_e$ , peaking roughly 6 s after Mg II. The onset of the  $N_e$  rise in the chromosphere and the transition region in the TC3 model is delayed roughly by 8 s after simulation start (orange curve in panel f). The atmosphere with  $T_{\text{init}} = 3 \text{ MK}$  is significantly denser than the 1 MK one (compare the black curves in panels e & f), leading to more efficient energy dissipation in the corona in the first  $\sim 6$  s (e.g. see Section 4.1 in Polito et al. 2018). Just like in the TC2 model, the intensities of both lines start to rise simultaneously, but the Mg II lightcurve shows a steeper increase and peaks first.

In summary, the analysis presented above suggests that the observed increase of Si IV emission before Mg II is reproduced in models with rapid density (and hence emission measure) enhancements in the transition region that occur prior to the equivalent increases in the chromosphere. This condition is rarely met in most of the EB models apart from those with a large energy flux density, or a very small  $E_c$ . The latter is however inconsistent with (or below the sensitivity of) *Fermi*/GBM observations (Table 1). The rapid density increase in the transition region is reproduced in the AW simulations, where the chromospheric increase is more gradual. None of the TC heating models in our parameter survey satisfy this requirement, because it takes longer for the density in the transition region to rise via the evaporation process to values high enough for the Si IV line to become visible and eventually peak.

### 5.5. Comparing flare dynamics from different energy transport mechanisms

Comparing the atmospheric evolution from simulations that are more consistent with the observed Si IV and Mg II delays can further guide us as to why these delays exist. Figure 10 presents a comparison from sample models that do (columns of panels a & c) and do not (columns of panels b & d) reproduce the observed delays. The parameter evolution is plotted between the heights  $z = 400 - 3000$  km, providing a detailed view of the chromosphere, transition region, and the lower corona. The figure uses the same color-coding as Figure 9. Top rows indexed ‘1’, ‘2’, and ‘3’ detail the evolution of gas temperature, electron number density ( $N_e$ ), and pressure, respectively. The macroscopic plasma velocity is plotted in row ‘4’, where positive values correspond

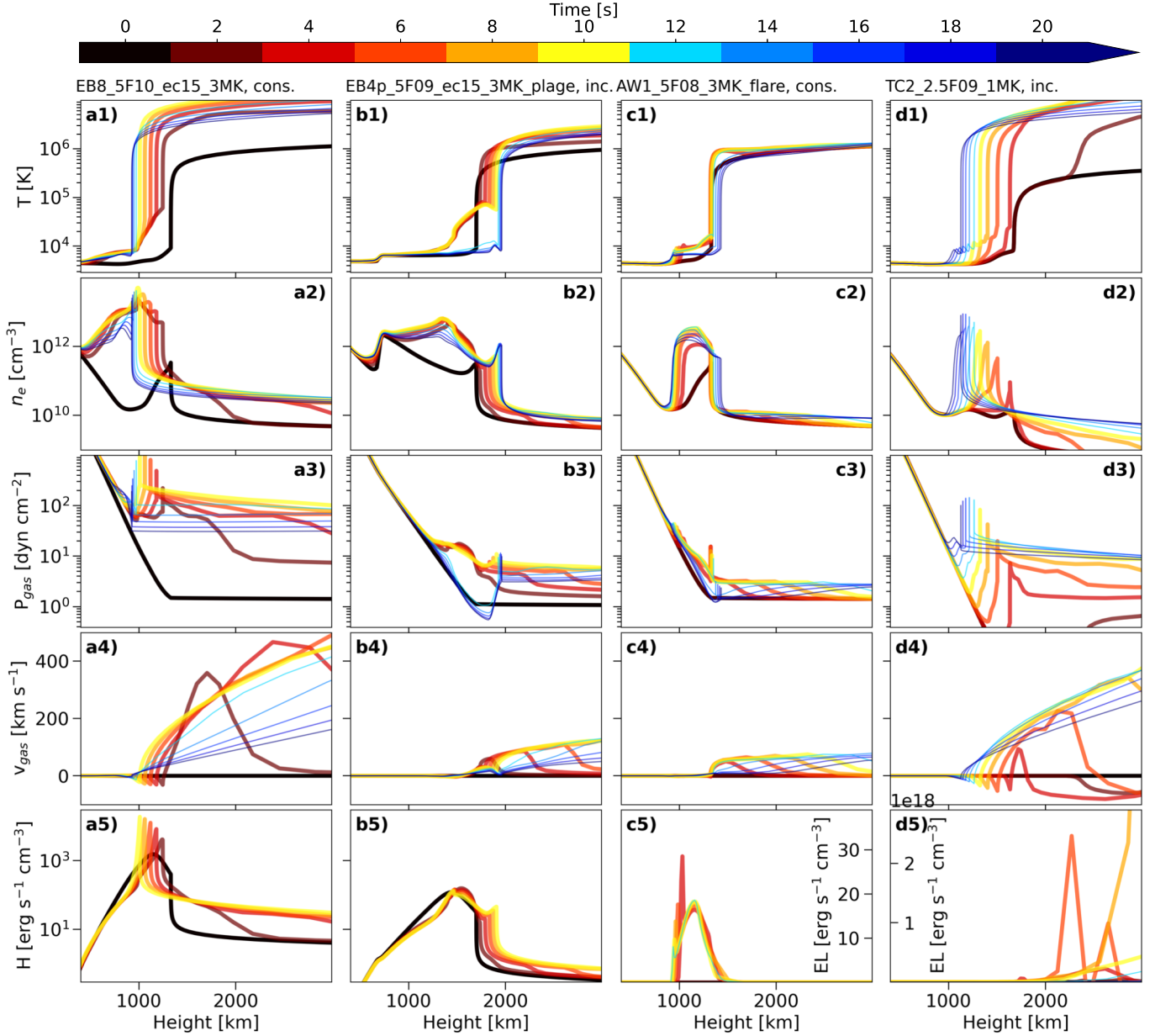


**Figure 10.** Spatio-temporal evolution of atmospheric parameters in example RADYN atmospheres. The color-coding was used to mark the time in the simulation with 2 s increments, starting from the initial state (black), the heating period (brown  $\rightarrow$  yellow thick curves), followed by the cooling period (cyan  $\rightarrow$  dark blue thin curves). Panels a and c present the models EB8 and AW1 that reproduce the observed positive delays between the Si IV and Mg II emission. Panels b and d show the evolution in the EB4p and TC2 models which are not consistent with the observations. From top to bottom are: gas temperature  $T$ , electron number density  $N_e$ , gas pressure, bulk velocity, and energy terms. This is expressed in terms of the EB heating  $H$  (in  $[\text{erg s}^{-1} \text{cm}^{-3}]$ , panels a5 and b5) and the energy losses due to heating (normalized, in  $[\text{erg s}^{-1} \text{cm}^{-3}]$ ) plotted in panels c5, d5.

to upflows. The last row ('5') presents energy terms expressed in terms of the EB heating (panels a& b) and energy losses ('EL') due to heating (panels c & d).

- **Consistent Model 1:** The energy deposition rate (panel a5) in the EB8 model exhibits a narrow maximum in the transition region, whose tails extend to the upper chromosphere as well as the corona. As a result of the heating, the temperature, density, and pressure exhibit a prompt (at  $t = 2$  s, brown color) rise in the entire region under study (panels a1 – a3). The region where the transition region forms shifts from  $\sim 1300$  km at the simulation onset to  $\sim 900$  km at the end of the investigated period. Strong density gradients and a pressure pulse are formed at the transition region at  $t = 4$  s, both

propagating downwards. The increase of pressure drives strong ( $v_g \sim 400 \text{ km s}^{-1}$ , panel a4) evaporative upflows above the transition region immediately after the onset of the heating.

- **Inconsistent Model 1:** The energy deposition in the EB4p simulation exhibits a broader peak spanning from the chromosphere to the transition region, peaking in the upper chromosphere at  $z \sim 1500 \text{ km}$  (panel b5). The order-of-magnitude EB flux decrease, compared to the EB8 model, translates to an order of magnitude drop in the peak heating. The temperature, density, and pressure increase at chromospheric altitudes (panels b1 – b3;  $z \sim 1700 \text{ km}$ ) are evident, while the position of the transition region shifts slightly upwards by  $\sim 200 \text{ km}$ . The pressure exhibits an increase in the chromosphere and, after  $t = 6 \text{ s}$ , a weak pulse in the transition region, driving modest evaporative flows with  $v_g \lesssim 100 \text{ km s}^{-1}$  above it.
- **Consistent Model 2:** The Alfvén wave heating in the AW1 model causes energy losses over a broad region below the transition region, with a narrow peak in the lower chromosphere at  $t = 4 - 8 \text{ s}$ . The  $\sim 4 \text{ s}$  delay of the energy losses after the start of the heating (panel c5) is caused by the wave travel time after injection. Unlike the rest of the models discussed here, the simulation shows only a modest temperature increase, both in the chromosphere and the lower corona ( $T_g \sim 10^6 \text{ K}$ , panel c1). The density in the transition region peaks at  $t = 4 - 6 \text{ s}$  after which it starts to slowly decrease as the location of the wave heating “bores” deeper into the chromosphere, as discovered by Reep et al. (2018). The fact that the wave propagates as opposed to traveling effectively instantaneously like the electron beams means that the chromospheric density peak is delayed until the end of the heating period (orange & yellow curves in panel c2). The weak pressure pulse in the transition region drives slow evaporation at  $v_g \lesssim 80 \text{ km s}^{-1}$  in the corona (panels c3 & c4). We also found that at  $t = 6 \text{ s}$ , the transition region position shifts slightly downward by  $\sim 3 \text{ km}$ , followed by the formation at progressively higher altitudes after  $t = 8 \text{ s}$ .
- **Inconsistent Model 2:** The *in-situ* direct heating in the model TC2 at altitudes  $z > 2000 \text{ km}$  causes significant (by more than an order of magnitude) temperature increase in the corona (panel d1) and steepens the temperature gradient in the transition region. The heating leads to a pressure gradient in the transition region which shifts down (to higher column masses) to balance the incoming conduction flux. The pressure gradient causes the temperature and density in the underlying chromosphere to rise at  $t \sim 6 \text{ s}$  (red curve in panels d1 & d2). The temperature continues to grow during the rest of the heating period (orange  $\rightarrow$  yellow curves), although gradual increase of the density and pressure progresses even beyond (panels d2 & d3). Pronounced pressure pulse drives evaporative upflows above the transition region, whose strength rises from  $v_g \sim 100 \text{ km s}^{-1}$  at  $t = 4 \text{ s}$  to  $v_g > 200 \text{ km s}^{-1}$  at  $t = 6 \text{ s}$  (panel d4).

The formation of Si IV line emission is contingent upon electron number density increase in the transition region. The plasma that fills the transition region originates in the underlying chromosphere and is carried upward by the evaporative flows driven by pressure imbalance due to heating. The location of energy deposition has a major effect on the evolution of the atmospheric parameters, including the gas velocity. The peak of the heating rate coincides with the transition region for example in the EB8 (Figure 10a) and EB9p (not shown) models that reproduce the observed delays. In both of those types of non-thermal electron distributions (larger  $F$  or small  $E_c$ ), there are a greater number of low-energy electrons that are easily thermalized in the transition region. Atmospheres where the bulk of the heating is released in the chromosphere, such as the EB4p (Figure 10b) as well as most of the EB models exhibit a steep Mg II emission increase preceding that of Si IV, not consistent with the observations. Our analysis suggests that whichever of the two lines in the EB as well as the AW models peaks first is given by the location of energy dissipation. Such interpretation is not applicable for the TC simulations. Since the downward directed heat flux from the thermal conduction models must travel through the transition region prior to the chromosphere, one might expect the transition region emission increase prior to the chromospheric one. Our analysis (Figure 9e, Figure 10d) however challenges this view, as the density increase sets on soon after the heating onset in both the chromosphere and the transition region. While the TC heating effectively dissipates in the corona (even more so for the 3 MK model), the lower atmosphere responds to the heating by increasing radiative losses from the chromosphere, driving Mg II emission before Si IV. In conclusion, both the density and the location of the heating deposition are key to explain why the Si IV peaks before Mg II or vice-versa.

## 6. DISCUSSION

### 6.1. Intensity peaks and kernel motions

The observations in Section 4.2 showed that peaks along the Mg II k (2796.35 Å), C II 1334.53 Å, and Si IV 1402.77 Å intensity lightcurves appeared quasi-periodically, at periods between 16 – 18 s. Solar flare emission often exhibits time variations or pulsations that can display a quasi-periodic pattern over a broad range of timescales, commonly referred to as quasi-periodic

pulsations (QPPs) (see e.g. Nakariakov & Melnikov 2009; McLaughlin et al. 2018; Zimovets et al. 2021, and references therein). For examples of studies reporting on QPP periods close to those reported here, see e.g. Hayes et al. (2020); Kou et al. (2022). While a broad range of studies have investigated QPPs, their underlying physical drivers remain uncertain. This is in part because the term ‘QPP’ encompasses a wide variety of observational signatures with different characteristics and likely different origins. Commonly proposed physical mechanisms include magnetohydrodynamic (MHD) waves, and ‘bursty’, time-dependent or oscillatory reconnection. QPPs may also originate in the upper reconnection region via instabilities or MHD wave-driven modulation of the reconnection rate (see discussions in Hayes et al. 2019; Kou et al. 2022). Oscillations of Si IV non-thermal broadening (Jeffrey et al. 2018) and intensity (Chitta & Lazarian 2020) with periods of about 10 s have also been previously interpreted as signatures of turbulence. However, with the exception of the event B2 when signal was strong, we did not find evidence for broadening increases associated to the intensity peaks in the event under study, suggesting that turbulence is unlikely to be the primary driver here. By investigating SJI 1330 Å intensities in ribbon portions adjacent to the IRIS slit, we found that the signal enhancements were caused by kernel brightenings either appearing or moving across the IRIS slit as a consequence of slipping reconnection, as further investigated in Lörinčik et al. (2025). QPPs driven by or associated to apparent slipping motions have been reported in the past at periods of a few minutes (Li & Zhang 2015) down to  $\approx 10$  s (Zhang et al. 2025), close to the timescales we report on here. While a detailed investigation into the origin of these QPP signatures is beyond the scope of this work, it represents a valuable direction for future research.

Since the dataset under study was acquired in the sit-and-stare mode, our analysis was limited to several IRIS pixels coincident with the ribbon portion where these kernels induced spectral enhancements. Given the orientation of the IRIS slit with respect to the ribbon, it is difficult to state how general these results are across the entirety of the flare. However, comparable behavior was observed across four distinct brightening events (B1 – B4), increasing credibility of our results. It ought to be emphasized that the cadence of conventional IRIS raster observations would not be high enough to resolve the delays between the chromospheric and the transition region emission. This highlights the importance of spectral measurements covering a large spatial region simultaneously and at a high cadence by instruments such as the upcoming Multi-slit Solar Explorer (MUSE; De Pontieu et al. 2022; Cheung et al. 2022) or the proposed Spectral Imager of the Solar Atmosphere (SISA; Calcines Rosario et al. 2024).

### 6.2. Delays and HXR signatures of particle acceleration

Despite the ubiquitous reconnection manifestations in the form of kernel motions (Section 3), the HXR observations from *Fermi*/GBM showed evidence of a weak non-thermal component only (Figure 1b). The non-thermal event set on  $\approx 2$  minutes after the first brightening event B1 had already occurred. Therefore, our interpretation of processes causing the observed delays (Section 5.4, 5.5) is likely only relevant to the time period coincident with the B2 – B4.

Examples of simulations reproducing the observed delays between the Si IV and Mg II peaks include the EB7 – EB8p atmospheres heated by high non-thermal EB flux. The  $F = 5 \times 10^{10}$  ergs cm<sup>2</sup> s<sup>-1</sup> used in those models is the upper constraint on the flux obtained from  $A_{\min}$  during B2. This result implies that, for the EB models to reproduce the observed delays, the non-thermal energy needs to be deposited to a small-scale ( $\sim 15$  IRIS pixels<sup>2</sup>) flare kernel (see also Section 2.2). The elevated flux levels were measured soon after the onset of the non-thermal event (Table 1), and therefore the high-flux models are relevant in the period coincident with the brightening event B2. Considering that the non-thermal flux decreased by a factor of  $\approx 20$  during the B2 and B4, but the delays were still mostly positive in the same period (Figure 5), indicates that the driver of these delays was likely changing during the flare.

Unlike the high-flux EB and Alfvén wave models, the EB9 and EB9p models reproduce both the observed delays and most of the observed spectral properties (Section 5.3). Although this is an interesting result, it has to be taken with caution as  $E_c = 5$  keV used therein is much lower than the  $E_c = 15$  keV adopted from the HXR spectral fitting. These models have been included in the analysis to explore the possibility of the delays being a consequence of heating by less energetic electrons with  $E_c$  below the detection threshold of *Fermi*/GBM (8 keV).

### 6.3. Open questions in delay simulations

Only a fraction of the RADYN models reproduce the observations (Section 5.2). The delays thus pose tight, previously unexplored constraints on RHD simulations of flare emission. In Figure 7, the positive delays reproduced in some of the electron-beam heated models (symbols) are clustered at  $\delta_t = 3.5, 6.5$  s, whereas the observed delays are distributed more uniformly. This clustering can be attributed to similar time evolution of these model atmospheres, where the electron density increase in the line formation regions sets on close in time. Differences of peak times of emission synthesized therein, if any, are below the 0.5 s temporal resolution of the synthetic lightcurves. None of the models reproduce the observed delays of  $\Delta_t/2 < \delta_t \lesssim 3$  and  $\approx 5$  s. A broader heating parameter survey would possibly fill this gap, but reproducing the exact properties of the observed delays was not the goal of this work.

Most of the lightcurves synthesized in the EB models, including those that reproduce the observed delays between the Si IV and Mg II emission, are characterized by steep intensity increase right after the heating onset (Figure 6). This behavior does not align with the observed lightcurves where the peaks exhibit gradual intensity increase and decrease, albeit with varying slopes, widths, and amplitudes (see Section 4.2 and Appendix D). Time evolution aligning with the observations is exhibited by the smoother lightcurves synthesized in the TC models (Figure 6u – y) which however do not reproduce the observed delays. An interesting result of its own, even though conduction fronts pass the transition region before reaching the chromosphere, the chromospheric emission is the first to rise and peak. This is due to the fact that the increase of the electron density in the transition region is driven by evaporation from the chromosphere which is the first to respond to *in-situ* heating in the corona by increasing radiative losses therein (see also Polito et al. 2018). Because of the efficient heating dissipation in the corona, especially in the 3 MK loops, the density increase in the transition region is delayed and the synthetic Si IV intensities in some cases peak as long as 20 s after the heating onset (Figure 6w). These lightcurves in addition last for tens of seconds, and the up to 15 s long delays between the Si IV and Mg II intensity peaks synthesized therein are much longer than the observed ones. We therefore conclude that it is unlikely for TC heating to reproduce the observed delays. Note that using an even higher initial loop apex temperature of 5 MK results in more effective dissipation in the corona and, as a consequence, reduced heating of the transition region, as shown in simulations of Polito et al. (2018). Relatively-shorter ( $< 3$  s) delays between the Mg II and trailing Si IV emission were found in TC-heated nanoflare loop models of Polito et al. (2018) that we revisited in our investigation (not shown). The 15 Mm loop length used in those simulations likely facilitates quicker post-evaporation density increase in the transition region compared to the 50 Mm loop length in the model grid constrained by our observations.

The last heating mechanism analyzed in our study are the Alfvén waves (AW). The lightcurves produced via two out of three AW-heated simulations under study were found to replicate the observed delays, with the Si IV line peaking first. The Si IV intensity lightcurve synthesized in the AW1 model also exhibited a relatively-gentle increase to the maximum (Figure 6z), in line with the observations. The AW models that reproduced the delays, on the contrary, did not replicate Si IV redshifts and broadening characteristic for the flare (although broadening due to the wave itself was not synthesized). Mild ( $v_D < 10$  km s<sup>-1</sup>) Si IV redshifts were found in the higher-flux AW3 model, which however does not reproduce the observed delays (Figure 6zb). When the atmospheric evolution therein (not shown) is compared to the lower-flux AW1 model (Figure 10c), the peak of the energy losses shifts to the chromosphere which also exhibits a strong increase of the electron number density. It ought to be noted that none of the simulations analyzed here account for persistent mild ( $v_D \lesssim 15$  km s<sup>-1</sup>) redshifts ubiquitous in transition region spectra (see e.g. Peter 1999; Peter & Judge 1999; Feldman et al. 2011, and references therein). Had these ‘reference’ redshifts been added to the synthetic spectra (Figure 8), the resulting Doppler shifts in the AW runs would align with the observations. Interestingly, the Alfvén wave models replicated the observations fairly well with no bespoke adjusting in otherwise broad parameter space of wave frequency  $f$ , perpendicular wavenumber  $k_x$  and magnetic field stratification. The chosen values of  $f$  and  $k_x$  were selected based on previous experience, as realistic values likely to produce damping near the transition region and in the upper chromosphere (Emslie & Sturrock 1982; Russell & Fletcher 2013; Reep & Russell 2016; Kerr et al. 2016; Russell 2024). Meanwhile, the magnetic field stratification had photospheric  $B_0 = 1500$  G and coronal  $B_{\text{cor}} = 500$  G (c.f. Eq. (10) of Kerr et al. (2016)) representing the upper constraint on the magnetic field strength in the active region (Section 5.1). The lack of precise measurements of coronal magnetic fields during flares poses a limitation on constraining the AW heating parameters. This has an impact on the Alfvén speed and wave damping properties. Spectral synthesis in RADYN simulations subjected to updated AW heating with different heating parameters will be presented in the follow-up study by Kerr et al. (2025).

We finally have to reiterate numerous assumptions and limitations of our experiment. First, Mg II line profiles synthesized in most RADYN+RH models are typically double-peaked, in contrast to single-peaked profiles commonly observed during flares, making comparisons between modeling and observations difficult. Next, even though the observed intensity peaks appeared quasi-periodically, all models considered in our study for simplicity assume a single instance of constant heating as we are here focused on simulating individual impulsive peak episodes in a single loop. Whether repeated heating of a single loop can reproduce the quasi-periodic intensity peaks delayed across different ions remains to be simulated in the future. In addition to these assumptions, we can not rule-out the possibility of coexistence of different non-thermal electron populations heating the same or adjacent volumes of plasma (Polito et al. 2023a), or simultaneous occurrence of different energy transport mechanisms. Last, the simulations under study are neither multithreaded (Falewicz et al. 2015; Polito et al. 2019; Reep et al. 2020), nor account for cross-sectional expansion of flux tubes (Reep et al. 2024), properties important for replicating flare lightcurves or description of mass flows from the chromosphere into the corona, respectively.

## 7. SUMMARY

This manuscript presents spectral analysis of the Si IV 1402.77 Å, C II 1334.53 Å, and Mg II 2796.35 Å lines observed by the IRIS satellite during a C-class flare from 2022 September 25. Line intensity lightcurves observed in periods coincident with the appearance of flare ribbon kernels beneath the IRIS slit exhibited multiple peaks. The most notable outcome of this study is the discovery of delays between the peaks along the intensity lightcurves. The delays between the transition region Si IV and the chromospheric Mg II line, we focused on primarily, were on average 1.8 s and up to  $\approx 6$  s long. Data indicate that the positive delays (Si IV peaks before equivalent Mg II peaks) were becoming more consistent as the time went by in the impulsive phase of the flare. These delays present an intriguing observable indicative of sequential excitation of different regions of the lower atmosphere of the Sun subjected to flare energization.

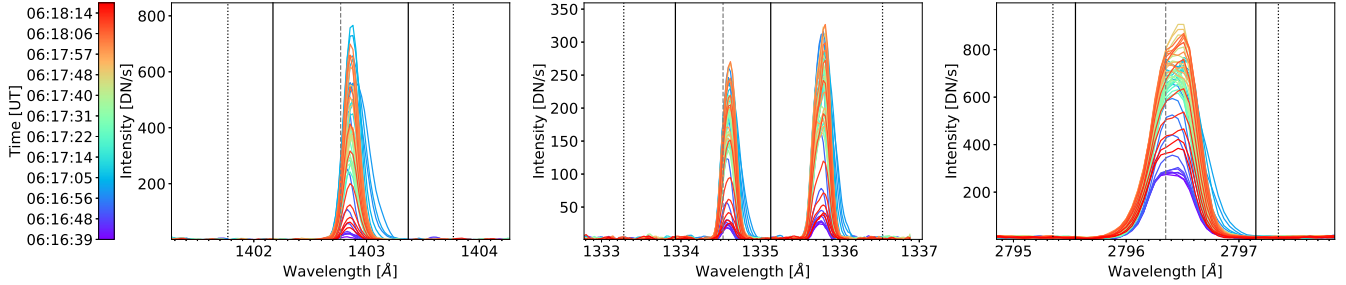
In order to investigate physical conditions leading to the delays revealed by the high-cadence IRIS spectroscopy, we analyzed a grid of RADYN flare atmospheres heated by electron beams, thermal conduction following *in-situ* heating in the corona, and Alfvén waves. Parameters of electron beam heating were constrained from HXR observations of *Fermi*/GBM, which detected a weak ( $E_c \approx 15$  keV) non-thermal event during the flare impulsive phase. Synthetic lightcurves consistent with the observations were reproduced in the high-flux ( $F = 5 \times 10^{10}$  ergs cm<sup>2</sup> s<sup>-1</sup>) electron beam and hybrid models, low flux ( $F = 1 \times 10^9$  ergs cm<sup>2</sup> s<sup>-1</sup>) but small  $E_c = 5$  keV models, and certain models heated by Alfvén waves. Simulation analysis revealed that the peaks in the Si IV emission precede their Mg II counterparts when the flare heating causes rapid and significant density increase from pre-flare levels in the transition region where Si IV forms. On the contrary, heating causing strong density increase in the chromosphere prior to the transition region causes Mg II intensity to increase before Si IV, which does not align with the observations. Model atmospheres heated by thermal conduction were found to be inconsistent with the observations as the Mg II emission precedes that of Si IV due to increased radiative losses in the chromosphere in the wake of *in-situ* coronal heating. Alfvén wave heating presents a promising candidate mechanism reproducing the observed delays, but the properties of synthetic spectra do not align with the observations and the wave parameters can be difficult to constrain. We have however just started to explore the Alfvén wave heating using the RADYN code, and further investigation of this mechanism is needed. It ought to be noted that majority of the observed delays, especially later in the flare impulsive phase, occurred when the *Fermi*/GBM flux was low ( $F = 5 \times 10^8 - 10^9$  ergs cm<sup>2</sup> s<sup>-1</sup>), supporting the notion that the delays are due to smaller energetic heating events or the Alfvén waves. It is also likely that the heating mechanism causing the delays could have been changing as the time went by during the flare.

To conclude, the newly-observed delays between the chromospheric and transition region emission have a rich diagnostic potential to probe the response of the lower atmosphere to flare heating and provide valuable constraints on models of flare emission. Future studies leveraging now extensive database of IRIS flare observations at very high, sub-second cadence will address the prevalence of these delays and their implications for flare energetics.

#### ACKNOWLEDGMENTS

JL and VP acknowledge support from NASA under the contract NNG09FA40C (IRIS). JL also acknowledges support from the Heliophysics Guest Investigator (H-GI) Open grant 80NSSC24K0553. V.P. also acknowledges support from NASA H-GI grant No. 80NSSC20K0716. GSK acknowledges support from a NASA Early Career Investigator Program award (grant 80NSSC21K0460). L.A.H was supported by an ESA Research Fellowship during the main part of this research. She is now supported by a Royal Society-Research Ireland University Research Fellowship. This manuscript benefited from discussions held at a meeting of the International Space Science Institute team: “Interrogating Field-Aligned Solar Flare Models: Comparing, Contrasting and Improving,” led by Dr. G. S. Kerr and Dr. V. Polito. Resources supporting this work were provided by the NASA High-End Computing (HEC) Program through the NASA Advanced Supercomputing (NAS) Division at Ames Research Center GID s2306. IRIS is a NASA small explorer mission developed and operated by LMSAL with mission operations executed at NASA Ames Research Center and major contributions to downlink communications funded by ESA and the Norwegian Space Agency. SDO data were obtained courtesy of NASA/SDO and the AIA and HMI science teams. This research has made use of the Astrophysics Data System, funded by NASA under Cooperative Agreement 80NSSC21M00561. CHIANTI is a collaborative project involving George Mason University, the University of Michigan (USA), University of Cambridge (UK) and NASA Goddard Space Flight Center (USA).

#### APPENDIX



**Appendix Figure 1.** Si IV 1402.77 Å (left), C II 1334.53 Å (middle), and Mg II 2796.35 Å (right) line profiles during the brightening event B2. Dashed grey lines indicate the rest wavelengths of lines under study. Solid black lines delineate the spectral region used for the calculation of moments of each line, while the grey dotted lines border regions used for the subtraction of the FUV and NUV continua around the profiles.

### A. TYPICAL IRIS LINE PROFILES

Example Si IV 1402.77 Å (left), C II 1334.53 Å and 1335.66 Å (middle), and Mg II 2796.35 Å (right) spectral line profiles observed during the B2 are plotted in Appendix Figure 1. In each panel, the rest wavelengths are indicated using the dashed gray line, while the solid black lines indicate the limits for calculating the moments (Section 4.1). The dotted black lines designate the inner boundaries of spectral regions used for the FUV and NUV continuum estimation, with the outer boundary corresponding to the plotted edge of the spectral window. For typical values of the total intensities, Doppler velocities, and line broadening determined via the moment analysis see Section 4.1 and Figure 3.

### B. MG II K3 INTENSITIES

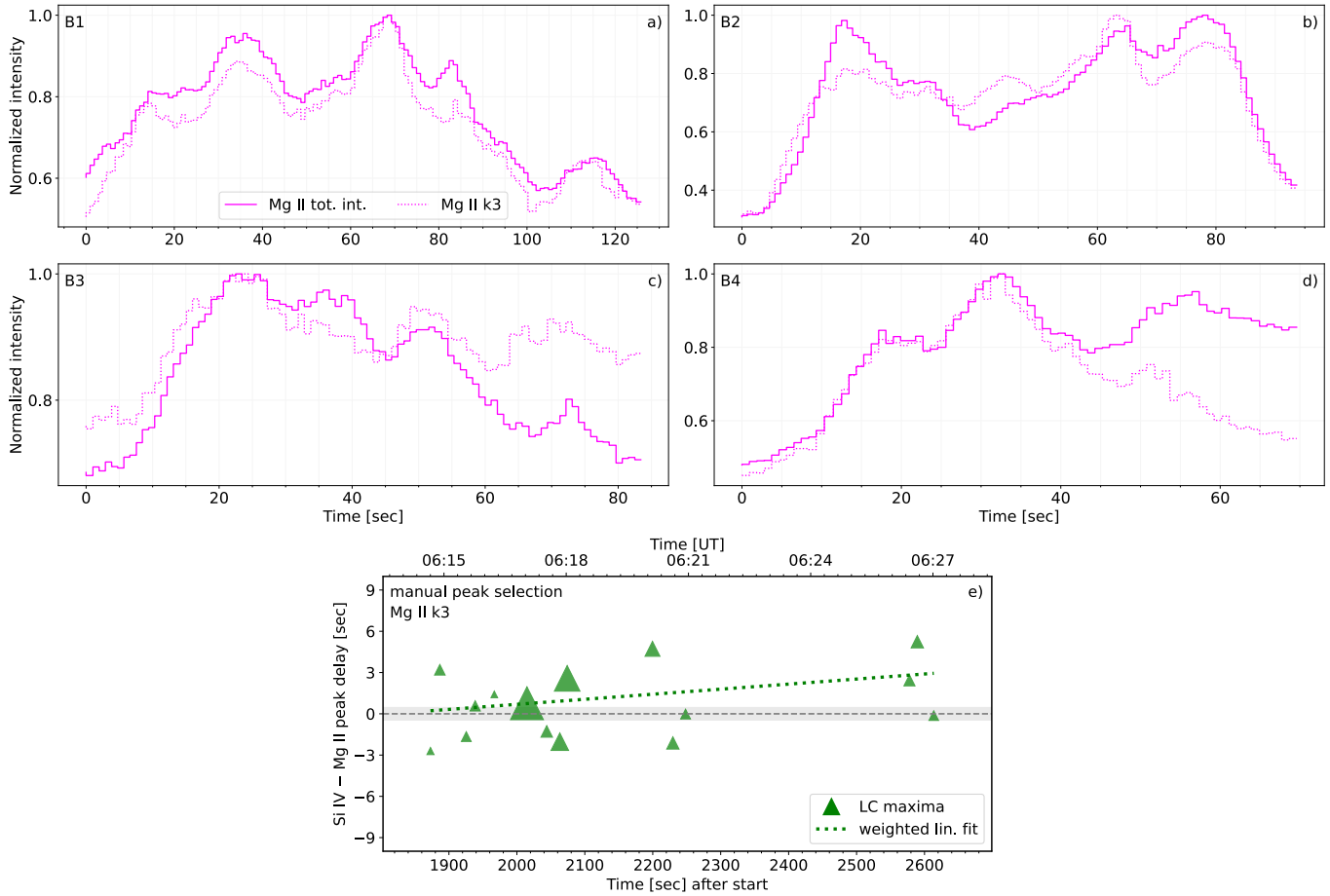
Unlike the typically single-peaked Si IV profiles, the Mg II spectra often consist of multiple components under quiescent conditions, or at certain flare locations (Polito et al. 2023a; Kerr et al. 2024b). The line core is commonly defined as k3 and the blue and red peaks as k2v and k2r, respectively. Only some of the analyzed profiles showed traces of these additional components, and most of the profiles were single-peaked (Appendix Figure 1), in agreement with previous analyses of Mg II flare characteristics in bright ribbons (e.g., Kerr et al. 2015; Panos et al. 2018; Polito et al. 2023a; Sainz Dalda & De Pontieu 2023). Nevertheless, the `iris_get_mg_features_lev2` (Pereira et al. 2013) was employed to probe the intensities and Doppler shifts of these components when they existed. Upon visual inspection of fits to the profiles we found that the line core or peak was typically well-fitted by the k3 component, and we focused on this component here. Appendix Figure 2a – d presents comparison of the Mg II intensities corresponding to the total (solid line) and k3 (dotted line) intensities during the B1 – B4. The k3 component lightcurves are generally similar to those of the total intensity, but they do not exhibit the same peaks and the peaks are in some cases less prominent, e.g. at  $t = 85$  s in panel a, or  $t = 20$  s in panel b. Further, the k3 lightcurve in panel c is noisier than the one corresponding to the total intensity.

The delays between the peak maxima along the Si IV total intensity lightcurves (Figure 4) and the Mg II k3 lightcurves are plotted in Appendix Figure 2e. This panel has the same style as Figure 5. The linear fit to the observed delays (green dotted line) is consistent with that of the integrated intensity plotted in Figure 5, albeit with more scatter around zero. The mean delay using the k3 intensities lowered to  $\delta_t = 0.7 \pm 0.6$  s with  $\sigma = 2.4$  s, while the mean positive delay is  $\delta_t = 2.6 \pm 0.6$  s with  $\sigma = 1.6$  s (see Appendix D for further details).

### C. AUTOMATIC DETECTION OF INTENSITY PEAKS

As stated in Section 4.2, the manual selection of the time intervals containing intensity peaks in different ions was in some cases difficult due to the characteristics of the peaks as well as presence of the noise. Peaks and peak intervals in the Si IV 1402.77 Å, Mg II k 2796.35 Å, and C II 1334.53 Å lightcurves were therefore also determined automatically using the `find_peaks` function of the SciPy library (Virtanen et al. 2020). Unlike our manual approach based on the identification of peak onset and end times (peak bases), this function directly returns positions and properties of peaks in an arbitrary signal.

Input parameters of this function include several criteria guiding the detection of the peaks, including their height, width, amplitude, or the mutual distance between the peaks. We found the method to yield the most reliable results when the peak detection was constrained by the minimal peak width of 2 time bins and the minimal separation between the peaks of at least 5 time bins. The performance of the method was negatively affected by the presence of the noise in the lightcurves, leading to false peak identifications. The lightcurves (intensities as well as their uncertainties) were therefore additionally smoothed using the Savitzky-Golay filter (`savgol_filter` function in SciPy) with a boxcar size of 5 time pixels. Once the peaks in the lightcurves

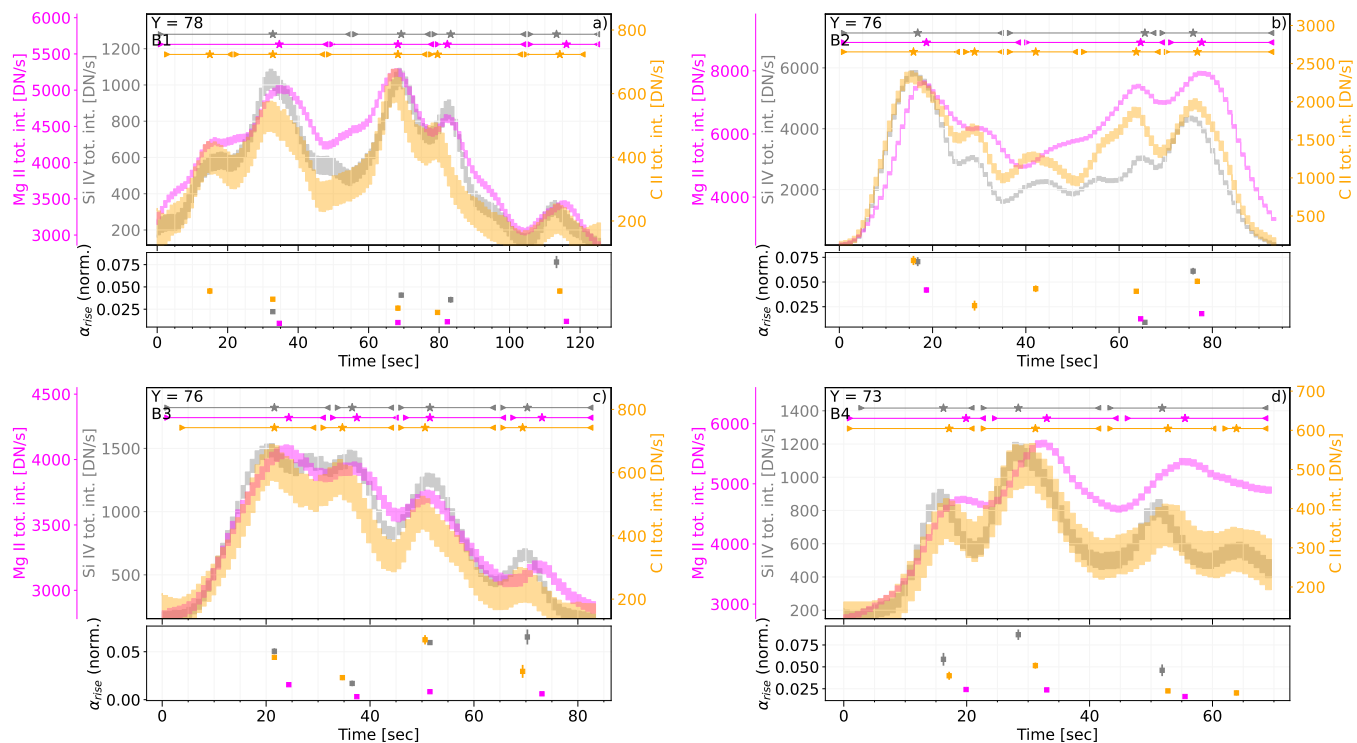


**Appendix Figure 2.** Comparison of normalized Mg II 2796.35 Å lightcurves obtained via computing the total intensities (0th moment, solid curves) and the k3 component (dotted curves) during the B1 – B4 (panels a – d). Panel e presents the delays between the maxima of Si IV and Mg II line intensity peaks a function of time during the flare. The panel has the same design as Figure 5, but the delays were computed using the Mg II k3 component intensities instead of the total intensity.

of the three lines have been identified, the peak bases were simply adapted from intensity minima in time intervals separating the detected peaks, or the peaks and the edges of the lightcurves. The peaks and peak intervals were subsequently used to measure the delays between the Si IV and Mg II k line emission (Appendix D).

The number of the automatically-identified peaks in lightcurves of different ions varied in few instances. While the delays between peak maxima can easily be obtained by comparing the peaks closest in time, the inconsistent time intervals need to be accounted for in the computation of the delays inferred from the centroid and cross-correlation methods (Appendix D). This was achieved by merging peak intervals in the lightcurves exhibiting a larger number of peaks over the same time interval. To illustrate this in a simplified example, if for example one ion exhibited one peak in the interval [0, 6], while the other showed two peak intervals at [0, 3] and [3, 6], the two intervals would coalesce into one longer interval [0, 6] containing two peaks. The algorithm essentially mimics our approach from the main analysis where matching (or similar) peak intervals across different ions were performed manually (Section 4.2).

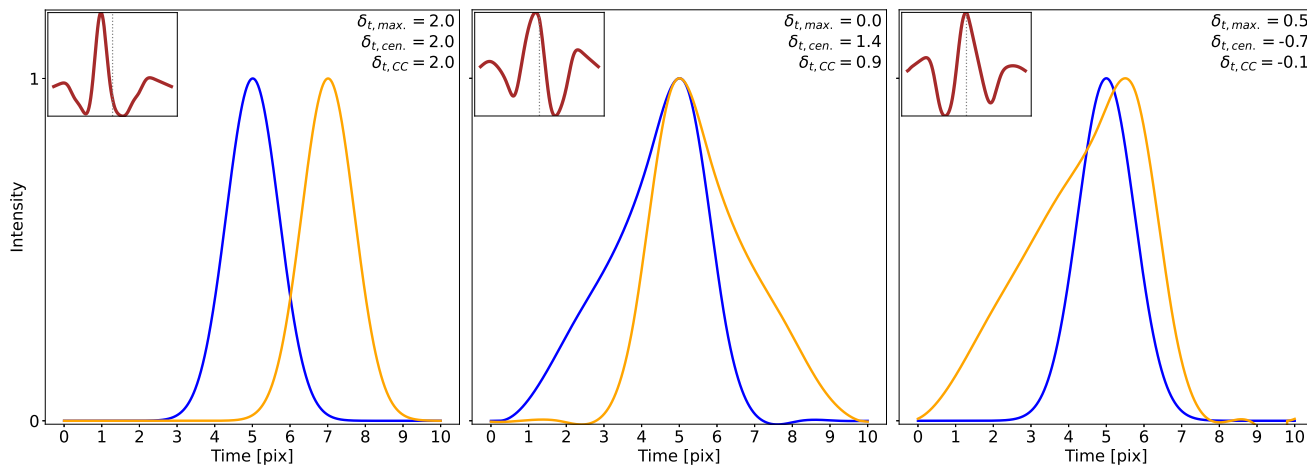
Appendix Figure 3 presents the smoothed lightcurves corresponding to the total line intensities, with peak intervals determined as disclosed above. The design and layout of the panels is identical to Figure 4; the upper portions of panels a – d present the lightcurves during the four brightening events B1 – B4, and their bottom parts show the slopes of the individual intensity peaks. Although the lightcurve smoothing resulted in a decrease of Si IV and Mg II peak detections during the B1 and B2 (panels a, b), the method identified an additional peak during the B3 (panel c). The ascending slopes of the Si IV and C II peaks are consistently larger than those of Mg II, what corresponds to the results described in Section 4.2 where the peaks and peak bases were selected manually. This means that the noise level, occasionally hindering the identification of the peak bases, did not affect the slope calculation and the conclusion drawn from this analysis. An exception to this trend is again visible in the case of the



**Appendix Figure 3.** Si IV 1402 Å (grey), Mg II 2796.35 Å (magenta), and C II 1334.53 Å (orange) line lightcurves during the B1 – B4 brightening events in the ribbon observed by IRIS. The lightcurves were smoothed over additional 5 time pixels compared to those in Figure 4. The colored horizontal bars above the lightcurves indicate automatically-identified peak intervals. The triangle symbols are the left and right bases (peak onset and end times), while the stars designate the maximum of each peak. The bottom part of each panel indicates the slopes of each peak after normalization.

single Mg II peak at  $t = 50 - 70$  s during the B2 (Appendix Figure 3b) where the method did not identify a low-amplitude Si IV peak at  $t \sim 55$  s (see Section 4.2 for details). The delays between the automatically-detected Si IV and Mg II peaks are plotted in Appendix Figure 5 and discussed in Appendix D.

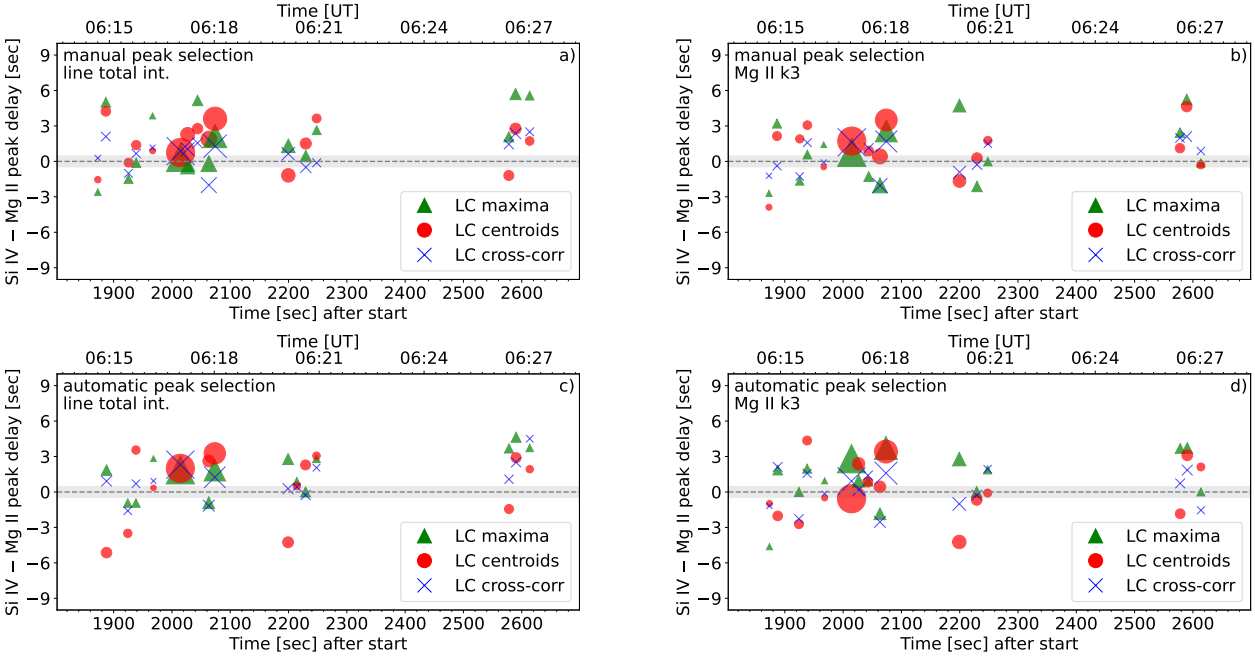
#### D. ADDITIONAL METHODS FOR INFERRING SI IV AND MG II DELAYS



**Appendix Figure 4.** Comparison of methods employed to infer the peak times between intensity peaks on selected pairs of functions. See Appendix D for details.

Subtraction of peak times is likely the easiest and the most straightforward way to quantify the delays between the intensity peaks. This method does not account for sometimes complicated time evolution of the individual peaks (Section 4.2). We have therefore extended our study by calculating the delays between the centroids of the peaks determined from the 1st moment in each time interval limited by the peak bases. The analysis is also complemented by cross-correlating the individual peak intervals observed in the two lines. The cross-correlations were performed using functions available within the `sunkit.image` library (Freij et al. 2023), see Barnes et al. (2019) for the method. The time lag between the intensity peaks in different ions in the corresponding time interval were inferred from a single-Gaussian fit to the core of the cross-correlation function. In cases where the shape of the cross-correlation function could not be approximated by a Gaussian, the time lag was adapted from the maximum of the cross-correlation function. Differences between the peak delays inferred using the selected methods are demonstrated on three pairs of functions with distinct time evolution, plotted in Appendix Figure 4. The insertion in the top-left corner of each panel represents the cross-correlation function of the two signals.

- The left panel depicts two Gaussians, blue one peaking at time  $t = 5$  s and the orange one peaking later at  $t = 7$  s. All three methods employed to study the delays between the intensity peaks show the same time delay  $\delta_t = 2$  s between the two signals.
- The middle panel presents two asymmetric signals whose maxima correspond to  $t = 5$  s. The blue signal is characterized by a gentle increase to its peak followed by a rapid decrease. The orange signal is a mirrored representation of the orange one; it peaks rapidly and then slowly decreases. This time evolution results in positive delays (blue signal ‘peaking’ first) inferred from the centroids  $\delta_{t, \text{cen.}}$  and the cross-correlation  $\delta_{t, \text{CC}}$ .
- The example presented in the right panel of Appendix Figure 4 shows a blue Gaussian and an orange asymmetric signal. Even though the blue Gaussian peaks before the orange signal ( $\delta_{t, \text{max}} = 0.5$  s) the initial rise of the orange signal results in small but negative delays inferred from the centroids and cross-correlations.



**Appendix Figure 5.** Delays between Si IV and Mg II k intensity peaks as a function of time during the flare. Panels a and b plot delays calculated in peak intervals determined manually. Automatic peak detection algorithm was used for the calculation of the delays plotted in panels c and d. Different symbols distinguish between the methods used for determining the peak times, and their size is given by the amplitude of Si IV peaks. Panels a and c present peak delays along lightcurves where both Si IV and Mg II k line intensities were obtained via the moment analysis. Mg II k3 component intensities were used for the calculation of delays plotted in panels b and d. The gray horizontal strip at  $t = 0$  s corresponds to  $\pm\Delta_t/2$ .

Appendix Figure 4 demonstrates the effects of slopes and symmetry of peaks on the delays inferred from the cross-correlations and peak centroids. The delays between the observed Si IV and Mg II intensity peaks inferred via the three methods differ

significantly for some peaks. Appendix Figure 5 presents the time evolution of the delays between Si IV and Mg II line emission during the impulsive phase of the flare. The figure has the same layout as Figure 5. The delays between the peak maxima (green triangles) are complemented by the delays inferred from peak centroids (red circles) and cross-correlations (blue crosses). The top row of Figure 5 a, b shows delays of peaks and peak intervals determined manually, while the automatic peak detection (Appendix C) was used to identify the peaks whose delays are plotted in panels c and d. Delays plotted in panels a, c were computed using the total line intensities, whereas the right column (panels b, d) shows the delays between the Si IV 1402.77 Å total intensity and the k3 component of the Mg II 2796.35 Å line.

The distribution of the datapoints in Appendix Figure 5 confirms that Si IV peaks typically occur before Mg II. This result holds regardless of the method used to

1. detect peaks and peak intervals (upper vs. bottom row),
2. measure Mg II k line intensities (left vs. right column),
3. infer peak time and/or peak delay (symbols).

The delays between the centroids (circles) of the automatically-detected peaks of the Si IV total intensity and the Mg II k3 component lightcurve, plotted in panel d, present an exception to this behavior. This is a result of additional smoothing and the fact that the k3 component intensity peaks were less prominent (Appendix C). The longest delays are typically found between peak maxima (triangles). Cross-correlating of the peak intervals, on the other hand, results in the lowest delays.  $\sim 60-85\%$  of the delays plotted in Appendix Figure 5 are lower than  $3\Delta_t$  ( $\approx 2.8$  s), depending on the method of Mg II k line intensity measurement and the peak selection method.

## REFERENCES

- Allred, J. C., Hawley, S. L., Abbett, W. P., & Carlsson, M. 2005, *ApJ*, 630, 573, doi: [10.1086/431751](https://doi.org/10.1086/431751)
- Allred, J. C., Kowalski, A. F., & Carlsson, M. 2015, *ApJ*, 809, 104, doi: [10.1088/0004-637X/809/1/104](https://doi.org/10.1088/0004-637X/809/1/104)
- Aulanier, G., Pariat, E., Démoulin, P., & Devore, C. R. 2006, *SoPh*, 238, 347, doi: [10.1007/s11207-006-0230-2](https://doi.org/10.1007/s11207-006-0230-2)
- Barnes, W. T., Bradshaw, S. J., & Viall, N. M. 2019, *ApJ*, 880, 56, doi: [10.3847/1538-4357/ab290c](https://doi.org/10.3847/1538-4357/ab290c)
- Brosius, J. W., & Holman, G. D. 2010, *ApJ*, 720, 1472, doi: [10.1088/0004-637X/720/2/1472](https://doi.org/10.1088/0004-637X/720/2/1472)
- . 2012, *A&A*, 540, A24, doi: [10.1051/0004-6361/201118144](https://doi.org/10.1051/0004-6361/201118144)
- Brosius, J. W., & Inglis, A. R. 2018, *ApJ*, 867, 85, doi: [10.3847/1538-4357/aae5f5](https://doi.org/10.3847/1538-4357/aae5f5)
- Brosius, J. W., & Phillips, K. J. H. 2004, *ApJ*, 613, 580, doi: [10.1086/422873](https://doi.org/10.1086/422873)
- Brown, J. C. 1971, *SoPh*, 18, 489, doi: [10.1007/BF00149070](https://doi.org/10.1007/BF00149070)
- Calcines Rosario, A., Auchère, F., Corso, A. J., et al. 2024, *Aerospace*, 11, 208, doi: [10.3390/aerospace11030208](https://doi.org/10.3390/aerospace11030208)
- Carlsson, M., Leenaarts, J., & De Pontieu, B. 2015, *ApJL*, 809, L30, doi: [10.1088/2041-8205/809/2/L30](https://doi.org/10.1088/2041-8205/809/2/L30)
- Carlsson, M., & Stein, R. F. 1992, *ApJL*, 397, L59, doi: [10.1086/186544](https://doi.org/10.1086/186544)
- . 1995, *ApJL*, 440, L29, doi: [10.1086/187753](https://doi.org/10.1086/187753)
- . 1997, *ApJ*, 481, 500, doi: [10.1086/304043](https://doi.org/10.1086/304043)
- Carlsson, M., Fletcher, L., Allred, J., et al. 2023, *A&A*, 673, A150, doi: [10.1051/0004-6361/202346087](https://doi.org/10.1051/0004-6361/202346087)
- Carmichael, H. 1964, *NASA Special Publication*, 50, 451
- Cheng, C. C., Tandberg-Hanssen, E., Bruner, E. C., et al. 1981, *ApJL*, 248, L39, doi: [10.1086/183619](https://doi.org/10.1086/183619)
- Cheung, M. C. M., Martínez-Sykora, J., Testa, P., et al. 2022, *ApJ*, 926, 53, doi: [10.3847/1538-4357/ac4223](https://doi.org/10.3847/1538-4357/ac4223)
- Chitta, L. P., & Lazarian, A. 2020, *ApJL*, 890, L2, doi: [10.3847/2041-8213/ab6f0a](https://doi.org/10.3847/2041-8213/ab6f0a)
- Czaykowska, A., Alexander, D., & De Pontieu, B. 2001, *ApJ*, 552, 849, doi: [10.1086/320553](https://doi.org/10.1086/320553)
- De Pontieu, B., Title, A. M., Lemen, J. R., et al. 2014, *SoPh*, 289, 2733, doi: [10.1007/s11207-014-0485-y](https://doi.org/10.1007/s11207-014-0485-y)
- De Pontieu, B., Polito, V., Hansteen, V., et al. 2021, *SoPh*, 296, 84, doi: [10.1007/s11207-021-01826-0](https://doi.org/10.1007/s11207-021-01826-0)
- De Pontieu, B., Testa, P., Martínez-Sykora, J., et al. 2022, *ApJ*, 926, 52, doi: [10.3847/1538-4357/ac4222](https://doi.org/10.3847/1538-4357/ac4222)
- Del Zanna, G., Dere, K. P., Young, P. R., & Landi, E. 2021, *ApJ*, 909, 38, doi: [10.3847/1538-4357/abd8ce](https://doi.org/10.3847/1538-4357/abd8ce)
- Dere, K. P., Landi, E., Mason, H. E., Monsignori Fossi, B. C., & Young, P. R. 1997, *A&AS*, 125, 149, doi: [10.1051/aas:1997368](https://doi.org/10.1051/aas:1997368)
- Dudík, J., Janvier, M., Aulanier, G., et al. 2014, *ApJ*, 784, 144, doi: [10.1088/0004-637X/784/2/144](https://doi.org/10.1088/0004-637X/784/2/144)
- Emslie, A. G., & Sturrock, P. A. 1982, *SoPh*, 80, 99, doi: [10.1007/BF00153426](https://doi.org/10.1007/BF00153426)
- Falewicz, R., Rudawy, P., Murawski, K., & Srivastava, A. K. 2015, *ApJ*, 813, 70, doi: [10.1088/0004-637X/813/1/70](https://doi.org/10.1088/0004-637X/813/1/70)
- Feldman, U., Dammasch, I. E., & Doschek, G. A. 2011, *ApJ*, 743, 165, doi: [10.1088/0004-637X/743/2/165](https://doi.org/10.1088/0004-637X/743/2/165)
- Fletcher, L. 2009, *A&A*, 493, 241, doi: [10.1051/0004-6361:20077972](https://doi.org/10.1051/0004-6361:20077972)
- Fletcher, L., & Hudson, H. S. 2008, *ApJ*, 675, 1645, doi: [10.1086/527044](https://doi.org/10.1086/527044)
- Fletcher, L., Dennis, B. R., Hudson, H. S., et al. 2011, *SSRv*, 159, 19, doi: [10.1007/s11214-010-9701-8](https://doi.org/10.1007/s11214-010-9701-8)
- Freij, N., Ireland, J., Mumford, S., et al. 2023, *sunpy/sunkit-image: v0.5.0, v0.5.0*, Zenodo, doi: [10.5281/zenodo.8234217](https://doi.org/10.5281/zenodo.8234217)
- Graham, D. R., Cauzzi, G., Zangrilli, L., et al. 2020, *ApJ*, 895, 6, doi: [10.3847/1538-4357/ab88ad](https://doi.org/10.3847/1538-4357/ab88ad)
- Haerendel, G. 2009, *ApJ*, 707, 903, doi: [10.1088/0004-637X/707/2/903](https://doi.org/10.1088/0004-637X/707/2/903)
- Handy, B. N., Acton, L. W., Kankelborg, C. C., et al. 1999, *Solar Physics*, 187, 229, doi: [10.1023/A:1005166902804](https://doi.org/10.1023/A:1005166902804)
- Harrison, R. A., Sawyer, E. C., Carter, M. K., et al. 1995, *SoPh*, 162, 233, doi: [10.1007/BF00733431](https://doi.org/10.1007/BF00733431)
- Hayes, L. A., Gallagher, P. T., Dennis, B. R., et al. 2019, *ApJ*, 875, 33, doi: [10.3847/1538-4357/ab0ca3](https://doi.org/10.3847/1538-4357/ab0ca3)
- Hayes, L. A., Inglis, A. R., Christe, S., Dennis, B., & Gallagher, P. T. 2020, *ApJ*, 895, 50, doi: [10.3847/1538-4357/ab8d40](https://doi.org/10.3847/1538-4357/ab8d40)
- Hirayama, T. 1974, *Solar Physics*, 34, 323, doi: [10.1007/BF00153671](https://doi.org/10.1007/BF00153671)
- Holman, G. D., Aschwanden, M. J., Aurass, H., et al. 2011, *SSRv*, 159, 107, doi: [10.1007/s11214-010-9680-9](https://doi.org/10.1007/s11214-010-9680-9)
- Hudson, H. S., Wolfson, C. J., & Metcalf, T. R. 2006, *SoPh*, 234, 79, doi: [10.1007/s11207-006-0056-y](https://doi.org/10.1007/s11207-006-0056-y)
- Jeffrey, N. L. S., Fletcher, L., Labrosse, N., & Simões, P. J. A. 2018, *Science Advances*, 4, 2794, doi: [10.1126/sciadv.aav2794](https://doi.org/10.1126/sciadv.aav2794)
- Kane, S. R. 1974, in *IAU Symposium*, Vol. 57, *Coronal Disturbances*, ed. G. A. Newkirk, 105
- Kašparová, J., Varady, M., Heinzel, P., Karlický, M., & Moravec, Z. 2009, *A&A*, 499, 923, doi: [10.1051/0004-6361/200811559](https://doi.org/10.1051/0004-6361/200811559)
- Kerr, G. S. 2022, *Frontiers in Astronomy and Space Sciences*, 9, 1060856, doi: [10.3389/fspas.2022.1060856](https://doi.org/10.3389/fspas.2022.1060856)
- . 2023, *Frontiers in Astronomy and Space Sciences*, 9, 1060862, doi: [10.3389/fspas.2022.1060862](https://doi.org/10.3389/fspas.2022.1060862)
- Kerr, G. S., Carlsson, M., Allred, J. C., Young, P. R., & Daw, A. N. 2019, *ApJ*, 871, 23, doi: [10.3847/1538-4357/aaf46e](https://doi.org/10.3847/1538-4357/aaf46e)
- Kerr, G. S., Fletcher, L., Russell, A. J. B., & Allred, J. C. 2016, *ApJ*, 827, 101, doi: [10.3847/0004-637X/827/2/101](https://doi.org/10.3847/0004-637X/827/2/101)
- Kerr, G. S., Kowalski, A. F., Allred, J. C., Daw, A. N., & Kane, M. R. 2024a, *MNRAS*, 527, 2523, doi: [10.1093/mnras/stad3135](https://doi.org/10.1093/mnras/stad3135)
- Kerr, G. S., Polito, V., Xu, Y., & Allred, J. C. 2024b, *ApJ*, 970, 21, doi: [10.3847/1538-4357/ad47e1](https://doi.org/10.3847/1538-4357/ad47e1)
- Kerr, G. S., Russell, A. J. B., Polito, V., et al. 2025, *In Prep.*

- Kerr, G. S., Simões, P. J. A., Qiu, J., & Fletcher, L. 2015, *A&A*, 582, A50, doi: [10.1051/0004-6361/201526128](https://doi.org/10.1051/0004-6361/201526128)
- Kopp, R. A., & Pneuman, G. W. 1976, *Solar Physics*, 50, 85, doi: [10.1007/BF00206193](https://doi.org/10.1007/BF00206193)
- Kou, Y., Cheng, X., Wang, Y., et al. 2022, *Nature Communications*, 13, 7680, doi: [10.1038/s41467-022-35377-0](https://doi.org/10.1038/s41467-022-35377-0)
- Křivský, L. 1963, *Bulletin of the Astronomical Institutes of Czechoslovakia*, 14, 77
- Lemen, J. R., Title, A. M., Akin, D. J., et al. 2012, *SoPh*, 275, 17, doi: [10.1007/s11207-011-9776-8](https://doi.org/10.1007/s11207-011-9776-8)
- Li, D., Ning, Z. J., & Zhang, Q. M. 2015, *ApJ*, 807, 72, doi: [10.1088/0004-637X/807/1/72](https://doi.org/10.1088/0004-637X/807/1/72)
- Li, T., & Zhang, J. 2015, *ApJL*, 804, L8, doi: [10.1088/2041-8205/804/1/L8](https://doi.org/10.1088/2041-8205/804/1/L8)
- Lin, R. P., & Hudson, H. S. 1976, *SoPh*, 50, 153, doi: [10.1007/BF00206199](https://doi.org/10.1007/BF00206199)
- Liu, W., Heinzel, P., Kleint, L., & Kašparová, J. 2015, *SoPh*, 290, 3525, doi: [10.1007/s11207-015-0814-9](https://doi.org/10.1007/s11207-015-0814-9)
- Liu, W.-J., Qiu, J., Longcope, D. W., & Caspi, A. 2013, *ApJ*, 770, 111, doi: [10.1088/0004-637X/770/2/111](https://doi.org/10.1088/0004-637X/770/2/111)
- Longcope, D. W. 2014, *ApJ*, 795, 10, doi: [10.1088/0004-637X/795/1/10](https://doi.org/10.1088/0004-637X/795/1/10)
- Lörinčík, J., Dudík, J., Sainz Dalda, A., et al. 2025, *Nature Astronomy*, 9, 45, doi: [10.1038/s41550-024-02396-4](https://doi.org/10.1038/s41550-024-02396-4)
- Lörinčík, J., Polito, V., De Pontieu, B., Yu, S., & Freij, N. 2022, *Frontiers in Astronomy and Space Sciences*, 9, 334, doi: [10.3389/fspas.2022.1040945](https://doi.org/10.3389/fspas.2022.1040945)
- McLaughlin, J. A., Nakariakov, V. M., Dominique, M., Jelínek, P., & Takasao, S. 2018, *SSRv*, 214, 45, doi: [10.1007/s11214-018-0478-5](https://doi.org/10.1007/s11214-018-0478-5)
- Meegan, C., Lichti, G., Bhat, P. N., et al. 2009, *ApJ*, 702, 791, doi: [10.1088/0004-637X/702/1/791](https://doi.org/10.1088/0004-637X/702/1/791)
- Nakariakov, V. M., & Melnikov, V. F. 2009, *SSRv*, 149, 119, doi: [10.1007/s11214-009-9536-3](https://doi.org/10.1007/s11214-009-9536-3)
- O'Dwyer, B., Del Zanna, G., Mason, H. E., Weber, M. A., & Tripathi, D. 2010, *A&A*, 521, A21, doi: [10.1051/0004-6361/201014872](https://doi.org/10.1051/0004-6361/201014872)
- Panos, B., Kleint, L., Huwylar, C., et al. 2018, *ApJ*, 861, 62, doi: [10.3847/1538-4357/aac779](https://doi.org/10.3847/1538-4357/aac779)
- Pereira, T. M. D., Leenaarts, J., De Pontieu, B., Carlsson, M., & Uitenbroek, H. 2013, *ApJ*, 778, 143, doi: [10.1088/0004-637X/778/2/143](https://doi.org/10.1088/0004-637X/778/2/143)
- Pereira, T. M. D., & Uitenbroek, H. 2015, *A&A*, 574, A3, doi: [10.1051/0004-6361/201424785](https://doi.org/10.1051/0004-6361/201424785)
- Pesnell, W. D., Thompson, B. J., & Chamberlin, P. C. 2012, *SoPh*, 275, 3, doi: [10.1007/s11207-011-9841-3](https://doi.org/10.1007/s11207-011-9841-3)
- Peter, H. 1999, *ApJ*, 516, 490, doi: [10.1086/307102](https://doi.org/10.1086/307102)
- Peter, H., & Judge, P. G. 1999, *ApJ*, 522, 1148, doi: [10.1086/307672](https://doi.org/10.1086/307672)
- Poland, A. I., Machado, M. E., Wolfson, C. J., et al. 1982, *SoPh*, 78, 201, doi: [10.1007/BF00151603](https://doi.org/10.1007/BF00151603)
- Polito, V., Del Zanna, G., Dudík, J., et al. 2016, *A&A*, 594, A64, doi: [10.1051/0004-6361/201628965](https://doi.org/10.1051/0004-6361/201628965)
- Polito, V., Kerr, G. S., Xu, Y., Sadykov, V. M., & Lorincik, J. 2023a, *ApJ*, 944, 104, doi: [10.3847/1538-4357/acaf7c](https://doi.org/10.3847/1538-4357/acaf7c)
- Polito, V., Peterson, M., Glesener, L., et al. 2023b, *Frontiers in Astronomy and Space Sciences*, 10, 1214901, doi: [10.3389/fspas.2023.1214901](https://doi.org/10.3389/fspas.2023.1214901)
- Polito, V., Testa, P., Allred, J., et al. 2018, *ApJ*, 856, 178, doi: [10.3847/1538-4357/aab49e](https://doi.org/10.3847/1538-4357/aab49e)
- Polito, V., Testa, P., & De Pontieu, B. 2019, *ApJL*, 879, L17, doi: [10.3847/2041-8213/ab290b](https://doi.org/10.3847/2041-8213/ab290b)
- Radziszewski, K., Rudawy, P., & Phillips, K. J. H. 2007, *A&A*, 461, 303, doi: [10.1051/0004-6361:20053460](https://doi.org/10.1051/0004-6361:20053460)
- . 2011, *A&A*, 535, A123, doi: [10.1051/0004-6361/200911924](https://doi.org/10.1051/0004-6361/200911924)
- Reep, J. W., & Russell, A. J. B. 2016, *ApJL*, 818, L20, doi: [10.3847/2041-8205/818/1/L20](https://doi.org/10.3847/2041-8205/818/1/L20)
- Reep, J. W., Russell, A. J. B., Tarr, L. A., & Leake, J. E. 2018, *ApJ*, 853, 101, doi: [10.3847/1538-4357/aaa2fe](https://doi.org/10.3847/1538-4357/aaa2fe)
- Reep, J. W., Scott, R. B., Chhabra, S., Unverferth, J., & Knizhnik, K. J. 2024, *ApJ*, 967, 53, doi: [10.3847/1538-4357/ad3c3c](https://doi.org/10.3847/1538-4357/ad3c3c)
- Reep, J. W., Warren, H. P., Moore, C. S., Suarez, C., & Hayes, L. A. 2020, *ApJ*, 895, 30, doi: [10.3847/1538-4357/ab89a0](https://doi.org/10.3847/1538-4357/ab89a0)
- Ricchiuzzi, P. J., & Canfield, R. C. 1983, *ApJ*, 272, 739, doi: [10.1086/161336](https://doi.org/10.1086/161336)
- Rubio da Costa, F., & Kleint, L. 2017, *ApJ*, 842, 82, doi: [10.3847/1538-4357/aa6eaf](https://doi.org/10.3847/1538-4357/aa6eaf)
- Rubio da Costa, F., Kleint, L., Petrosian, V., Liu, W., & Allred, J. C. 2016, *ApJ*, 827, 38, doi: [10.3847/0004-637X/827/1/38](https://doi.org/10.3847/0004-637X/827/1/38)
- Rubio da Costa, F., Kleint, L., Petrosian, V., Sainz Dalda, A., & Liu, W. 2015, *ApJ*, 804, 56, doi: [10.1088/0004-637X/804/1/56](https://doi.org/10.1088/0004-637X/804/1/56)
- Russell, A. J. B. 2024, in *Alfvén Waves Across Heliophysics: Progress, Challenges, and Opportunities*, ed. A. Keiling, Vol. 285, 39–73, doi: [10.1002/9781394195985.ch3](https://doi.org/10.1002/9781394195985.ch3)
- Russell, A. J. B., & Fletcher, L. 2013, *ApJ*, 765, 81, doi: [10.1088/0004-637X/765/2/81](https://doi.org/10.1088/0004-637X/765/2/81)
- Sainz Dalda, A., & De Pontieu, B. 2023, *Frontiers in Astronomy and Space Sciences*, 10, 1133429, doi: [10.3389/fspas.2023.1133429](https://doi.org/10.3389/fspas.2023.1133429)
- Sandlin, G. D., Bartoe, J. D. F., Brueckner, G. E., Tousey, R., & Vanhoosier, M. E. 1986, *ApJS*, 61, 801, doi: [10.1086/191131](https://doi.org/10.1086/191131)
- Simões, P. J. A., Reid, H. A. S., Milligan, R. O., & Fletcher, L. 2019, *ApJ*, 870, 114, doi: [10.3847/1538-4357/aaf28d](https://doi.org/10.3847/1538-4357/aaf28d)
- Sturrock, P. A. 1966, *Nature*, 211, 695, doi: [10.1038/211695a0](https://doi.org/10.1038/211695a0)
- SunPy Community, Barnes, W. T., Bobra, M. G., et al. 2020, *ApJ*, 890, 68, doi: [10.3847/1538-4357/ab4f7a](https://doi.org/10.3847/1538-4357/ab4f7a)
- Tandberg-Hanssen, E., Reichmann, E., & Woodgate, B. 1983, *SoPh*, 86, 159, doi: [10.1007/BF00157184](https://doi.org/10.1007/BF00157184)

- Testa, P., De Pontieu, B., Allred, J., et al. 2014, *Science*, 346, 1255724, doi: [10.1126/science.1255724](https://doi.org/10.1126/science.1255724)
- Torrence, C., & Compo, G. P. 1998, *Bulletin of the American Meteorological Society*, 79, 61, doi: [10.1175/1520-0477\(1998\)079<0061:APGTWA>2.0.CO;2](https://doi.org/10.1175/1520-0477(1998)079<0061:APGTWA>2.0.CO;2)
- Trottet, G., Rolli, E., Magun, A., et al. 2000, *A&A*, 356, 1067
- Uitenbroek, H. 2001, *ApJ*, 557, 389, doi: [10.1086/321659](https://doi.org/10.1086/321659)
- Virtanen, P., Gommers, R., Oliphant, T. E., et al. 2020, *Nature Methods*, 17, 261, doi: [10.1038/s41592-019-0686-2](https://doi.org/10.1038/s41592-019-0686-2)
- Švestka, Z. 1970, *SoPh*, 13, 471, doi: [10.1007/BF00153567](https://doi.org/10.1007/BF00153567)
- Wang, L. F., Li, Y., Li, Q., Cheng, X., & Ding, M. D. 2023, *ApJS*, 268, 62, doi: [10.3847/1538-4365/acf127](https://doi.org/10.3847/1538-4365/acf127)
- Warren, H. P., Reep, J. W., Crump, N. A., & Simões, P. J. A. 2016, *ApJ*, 829, 35, doi: [10.3847/0004-637X/829/1/35](https://doi.org/10.3847/0004-637X/829/1/35)
- Yu, K., Li, Y., Ding, M. D., et al. 2020, *ApJ*, 896, 154, doi: [10.3847/1538-4357/ab9014](https://doi.org/10.3847/1538-4357/ab9014)
- Zhang, Y., Li, T., Hou, Y., et al. 2025, *ApJL*, 982, L9, doi: [10.3847/2041-8213/adbb6e](https://doi.org/10.3847/2041-8213/adbb6e)
- Zimovets, I. V., McLaughlin, J. A., Srivastava, A. K., et al. 2021, *SSRv*, 217, 66, doi: [10.1007/s11214-021-00840-9](https://doi.org/10.1007/s11214-021-00840-9)
- Zirin, H. 1978, *SoPh*, 58, 95, doi: [10.1007/BF00152557](https://doi.org/10.1007/BF00152557)